



# Three-phase Interstellar Medium in Galaxies Resolving Evolution with Star Formation and Supernova Feedback (TIGRESS): Algorithms, Fiducial Model, and Convergence

Chang-Goo Kim<sup>ID</sup> and Eve C. Ostriker<sup>ID</sup>

Department of Astrophysical Sciences, Princeton University, Princeton, NJ 08544, USA; [cgkim@astro.princeton.edu](mailto:cgkim@astro.princeton.edu), [eco@astro.princeton.edu](mailto:eco@astro.princeton.edu)

Received 2016 December 9; revised 2017 August 7; accepted 2017 August 8; published 2017 September 11

## Abstract

We introduce TIGRESS, a novel framework for multi-physics numerical simulations of the star-forming interstellar medium (ISM) implemented in the Athena MHD code. The algorithms of TIGRESS are designed to spatially and temporally resolve key physical features, including: (1) the gravitational collapse and ongoing accretion of gas that leads to star formation in clusters; (2) the explosions of supernovae (SNe), both near their progenitor birth sites and from runaway OB stars, with time delays relative to star formation determined by population synthesis; (3) explicit evolution of SN remnants prior to the onset of cooling, which leads to the creation of the hot ISM; (4) photoelectric heating of the warm and cold phases of the ISM that tracks the time-dependent ambient FUV field from the young cluster population; (5) large-scale galactic differential rotation, which leads to epicyclic motion and shears out overdense structures, limiting large-scale gravitational collapse; (6) accurate evolution of magnetic fields, which can be important for vertical support of the ISM disk as well as angular momentum transport. We present tests of the newly implemented physics modules, and demonstrate application of TIGRESS in a fiducial model representing the solar neighborhood environment. We use a resolution study to demonstrate convergence and evaluate the minimum resolution  $\Delta x$  required to correctly recover several ISM properties, including the star formation rate, wind mass-loss rate, disk scale height, turbulent and Alfvénic velocity dispersions, and volume fractions of warm and hot phases. For the solar neighborhood model, all these ISM properties are converged at  $\Delta x \leq 8$  pc.

**Key words:** galaxies: ISM – galaxies: star formation – methods: numerical

## 1. Introduction

Feedback from massive young stars plays a crucial role in regulating star formation and the properties of the interstellar medium (ISM) at all scales (e.g., McKee & Ostriker 2007; Krumholz et al. 2014). Stellar winds and ionizing+non-ionizing radiation from massive stars profoundly affect their birth environment, and the large-scale outflows that these processes produce impose an upper limit on the lifetime star formation efficiency of the parent giant molecular cloud (GMC) (e.g., Lopez et al. 2014; Dale 2015; Raskutti et al. 2016). Protostellar outflows and jets driven in the course of low-mass star formation may also contribute to supporting the parent molecular cloud, and extending its life (e.g., Wang et al. 2010; Frank et al. 2014). When a massive star dies, the most extreme feedback event occurs, with the instantaneous release of  $\sim 10^{51}$  erg in the form of high-velocity supernova (SN) ejecta (e.g., Leitherer et al. 1999; Heger et al. 2003). Among the many forms of stellar feedback, SNe are believed to be the most important for driving turbulence of the warm and cold neutral media of the ISM (WNM and CNM, respectively) (e.g., Mac Low & Klessen 2004) and for regulating galactic star formation rates (SFRs) (e.g., Ostriker et al. 2010; Kim et al. 2011; Ostriker & Shetty 2011), as well as for creating the hot component of the ISM (e.g., Cox & Smith 1974; McKee & Ostriker 1977). The collective effects of many (spatially and temporally) correlated SNe create superbubbles that expand away from the disk midplane and contribute to driving galactic fountains and winds (e.g., Kim et al. 2017, and references therein). Expulsion of baryons in winds driven by star formation feedback are believed to play a critical role in shaping the galaxy stellar mass function, particularly in low-mass halos (e.g., Somerville & Davé 2015).

Although the importance of SN feedback to the ISM has long been recognized (e.g., McKee & Ostriker 1977), proper implementation in numerical simulations is challenging due to the requirements of very high spatial and temporal resolution. An SN releases prodigious energy that is extremely concentrated in both space and time. This produces high-velocity shock waves propagating into the surrounding gas, and the shocked ambient medium that comprises the interior of a SN remnant is extremely hot. At later stages, after the denser portion of the hot gas is able to cool, both individual SN remnants and superbubbles are bounded by shells of cooled, dense gas, while their interiors remain hot. Because the initial momentum of the SN ejecta is boosted (by more than an order of magnitude) during the energy-conserving stage by the work of the expanding hot bubble on the surrounding ISM, it is crucial to resolve this evolutionary stage (e.g., Cioffi et al. 1988; Thornton et al. 1998; Kim & Ostriker 2015a). For the remnant of an isolated SN propagating into gas of number density  $n = 100 - 0.1 \text{ cm}^{-3}$ , the energy-conserving Sedov-Taylor stage ends at the shell formation time  $t_{\text{sf}} \sim 10^3 - 10^5$  years, when the SN remnant radius is  $r_{\text{sf}} \sim 1 - 10$  pc. In order to obtain numerically converged results—in particular for the history of hot gas mass and the final radial momentum—these temporal and spatial scales must be resolved. Kim & Ostriker (2015a) found that convergence requires  $r_{\text{sf}}$  to be resolved by at least three grid zones, which imposes an upper limit on the initial size of the SN feedback region and the grid resolution  $\Delta x$ .

In cosmological galaxy formation simulations using current computational resources (where the best resolution is several tens of pc), it is generally not possible to resolve the Sedov-Taylor stage of individual SN remnants. Thermal energy

dumped into a scale larger than the expected  $r_{\text{sf}}$  (or shared with a larger mass than this radius would enclose) immediately cools away, and this feedback has no impact on subsequent star formation (e.g., Katz 1992). “Over-cooling” from unresolved SN feedback leads to overly efficient conversion of gas to stars, and galaxies that are too massive. To deal with the “over-cooling” problem in galaxy formation simulations, a wide variety of sub-grid models for treating feedback has been developed (e.g., Dalla Vecchia & Schaye 2012; Agertz et al. 2013; Teyssier et al. 2013; Hopkins et al. 2014; Kimm & Cen 2014). Many sub-grid models have been calibrated to reproduce basic observables, such as the stellar mass to halo mass relation (e.g., Behroozi et al. 2013; Moster et al. 2013), the Kennicutt-Schmidt relation (Kennicutt 1998), star formation history, and other properties (e.g., Hopkins et al. 2014; Vogelsberger et al. 2014; Crain et al. 2015; Schaye et al. 2015; Agertz & Kravtsov 2016; Davé et al. 2016; Keller et al. 2016).

While recent efforts have been successful in matching stellar abundances and SFRs, detailed gas properties in the ISM and also circumgalactic and intergalactic media (CGM and IGM, respectively) can differ substantially depending on the feedback treatment adopted. For example, in Rosdahl et al. (2017), delayed cooling and kinetic feedback approaches unphysically enhance the ratio of gas outflow rate to SFR (a.k.a. the mass-loading factor), altering the volume filling factors and compositions of the CGM and IGM. Approaches that accumulate sufficient energy from SNe that the temperature of the feedback region is high are able to limit cooling. However, from higher-resolution simulations, it is known that the spatial and temporal correlations (or de-correlations) of SNe with the gas can strongly affect the proportions of ISM mass and volume in different phases (e.g., Hennebelle & Iffrig 2014; Gatto et al. 2015; Li et al. 2015; Kim et al. 2017). “Accumulation” of feedback energy based on the resolution of simulation generally will not recover the true spacetime correlations of SN with each other and the ISM gas.

In intermediate-scale simulations, it is possible to incorporate detailed ISM physics and resolve SN feedback. Utilizing vertically stratified boxes that represent local patches in galactic disks, the roles of SNe in driving turbulence and shaping the multiphase ISM in galactic disks have been extensively investigated (e.g., Korpi et al. 1999; de Avillez 2000; de Avillez & Breitschwerdt 2004; Joung & Mac Low 2006; Hill et al. 2012; Gent et al. 2013; Walch et al. 2015; Girichidis et al. 2016; Li et al. 2017). Most studies to date have simply imposed an SN rate based on an empirical relationship between gas surface density and the surface density of star formation (e.g., the Kennicutt-Schmidt relation of Kennicutt 1998), and evolve the ISM subject to this fixed rate, setting off SNe at either random locations or loci restricted by their density. However, imposed feedback of this kind can lead to ISM states that are quite unphysical, e.g., with the hot medium occupying either a negligible volume or almost the entire domain. Instead, for self-consistency, the rate of star formation and SN explosions should be self-regulated, because SN feedback provides a strong negative feedback (e.g., Ostriker et al. 2010; Kim et al. 2011, 2013; Ostriker & Shetty 2011).

Only a few recent simulations have studied the effects of resolved SN feedback within models in which the SN rate in the three-phase ISM is self-consistently determined by collapse under self-gravity (Hennebelle & Iffrig 2014; Gatto et al. 2017; Peters et al. 2017). Furthermore, these simulations have had

relatively brief duration ( $\leq 100$  Myr) and do not appear to have reached a quasi-steady state in which the rates of star formation and feedback and the ISM properties are independent of initial conditions. These simulations have also neglected galactic differential rotation, which is responsible for limiting gravitational collapse at large scales (e.g., Kim et al. 2002) and creating and maintaining magnetic fields via galactic dynamos (e.g., Kim & Ostriker 2015b).

In this paper, we present a comprehensive framework for modeling the turbulent, magnetized, multiphase, self-gravitating ISM in a local, vertically stratified box with sheared rotation, including star formation and SN feedback. The TIGRESS (Three-phase Interstellar medium in Galaxies Resolving Evolution with Star formation and Supernova feedback) framework we have developed is designed to be applied in a wide variety of galactic environments. The investigation underway will produce detailed theoretical representations of the ISM and star formation properties for comparison to observations of the Milky Way and nearby galaxies. In addition, resolved TIGRESS simulations may be used to develop and calibrate sub-grid models for galaxy formation simulations in which direct resolution of the ISM, star formation, and feedback effects—including driving winds—is not possible.

To achieve the highest level of realism and predictive power in simulating the star-forming ISM, standard algorithms to evolve the equations of magnetohydrodynamics (MHD), solve for self-gravity, and apply heating and cooling must be coupled to a number of more specialized methods that represent key physical elements that are particular to the problem at hand. The specialized TIGRESS algorithms include treatment of local gravitational collapse and accretion onto sink/star particles representing clusters, and treatment of direct feedback to the ISM from sink/star particles in the form of SNe and photoelectric heating, based on a stellar population synthesis model. In addition to OB stars in clusters represented by sink/star particles, we model runaway OB stars ejected from these sites; both produce SNe. TIGRESS allows for three different types of SN feedback, representing different evolutionary stages of SN remnants, and the type applied depends on the ambient density surrounding the explosion site and the local grid resolution. In addition to explicitly following the energy-conserving stage of SN remnants (which is almost always possible at the typical grid resolution), TIGRESS allows for two other treatments of SNe that follow the momentum-conserving or the free-expansion stages of SN remnants (SNRs) when the ambient density is either very high or very low, respectively. In the former case, this captures the correct momentum injection by a SN to the surrounding ISM when the pre-radiative SN evolution is unresolved; in the latter case, this captures early evolution more correctly before thermalizing the interior of the SNR. In this paper, we describe the specialized TIGRESS algorithms (and tests of these methods) fully, so that the simulations we conduct will be reproducible by other groups.

To demonstrate the application of TIGRESS, we present results from a fiducial simulation with parameters similar to those of the solar neighborhood. This model runs long enough (three galactic orbits, or  $\sim 700$  Myr) that a fully self-consistent quasi-steady state is reached, with more than 10 self-regulation cycles of star formation. We show time histories of star formation and feedback loops, as well as basic gas properties including phase balance, turbulent velocities, magnetic field

strengths, and disk scale heights. The resulting ISM is highly realistic, with cold, warm, and hot phases; velocity dispersions and magnetic field strengths are also realistic.

In addition to simple tests of individual numerical modules, it is important to test the overall behavior of the complex, highly coupled nonlinear model system. An essential “system test” that is required in any complex application, and particularly any application involving turbulence, is the study of convergence with respect to numerical resolution. Previously, there have been resolution studies mainly focused on convergence in the mass fractions of the three thermal phases mediated by SN feedback (at fixed rates) in different models (e.g., de Avillez & Breitschwerdt 2004; Hill et al. 2012; Gent et al. 2013). In the present work, a significant advance is that the SN feedback rate is self-regulated (by the response of star formation to changes in the ISM induced by feedback), and the temporal/spatial correlations of SNe are realistic with respect to the various ISM phases. Systematic exploration of resolution effects and convergence criteria for the self-consistent TIGRESS implementation is required. We present a resolution study for the fiducial simulation, varying resolution from  $\Delta x = 2$  to 64 pc. We analyze convergence of several properties including the SFR, wind mass-loss rate, disk scale height, turbulent and Alfvénic velocity dispersions, and volume fractions of warm and hot phases.

The remainder of this paper is organized as follows. In Section 2, we describe our numerical algorithms. Section 2.2 describes treatment of sink/star particles (including creation, accretion, aging, and integration of motion). Section 2.3 describes feedback algorithms including our population synthesis treatment, treatment of FUV radiation/photoelectric heating (Section 2.3.1), and treatment of SN rates and energy injection prescriptions (Sections 2.3.2–2.3.3). In Section 3, we present results from our fiducial solar neighborhood model with spatial resolution of  $\Delta x = 4$  pc. In Section 4, we present a convergence study of the fiducial run with varying spatial resolution. Section 5 summarizes the paper.

## 2. Numerical Methods

### 2.1. Magnetohydrodynamic Equations and Additional Physics

We solve the ideal MHD equations in a local, shearing box (e.g., Stone & Gardiner 2010). The transformation maps from global cylindrical  $(R, \phi)$  coordinates to local Cartesian coordinates as  $(x, y) = (R - R_0, R_0[\phi - \Omega t])$ , where  $R_0$  is the galactocentric distance of the box center and  $\Omega$  is the angular velocity of galactic rotation at  $R_0$ . The vertical coordinate  $z$  remains global. Assuming galactic differential rotation with the shear parameter  $q \equiv -d \ln \Omega / d \ln R|_{R_0} = 1$  for a flat rotation curve, we have background shear velocity of  $v_s = -q\Omega x\hat{y}$ . In this local, rotating frame, inertial forces emerge in the form of the Coriolis force,  $-2\Omega \times v$ , and the tidal potential,  $\Phi_{\text{tidal}} = -q\Omega^2 x^2$ . Including gaseous and (young) stellar self-gravity, a fixed “external” gravitational potential to represent the old stellar disk and dark matter halo, and optically thin cooling and heating, the governing equations are given by

$$\frac{\partial \rho}{\partial t} + \nabla \cdot (\rho v) = 0, \quad (1)$$

$$\begin{aligned} \frac{\partial(\rho v)}{\partial t} + \nabla \cdot \left( \rho v v + P + \frac{B^2}{8\pi} - \frac{\mathbf{B}\mathbf{B}}{4\pi} \right) \\ = -2\Omega \times (\rho v) - \rho \nabla \Phi_{\text{tot}}, \end{aligned} \quad (2)$$

$$\begin{aligned} \frac{\partial}{\partial t} \left( \frac{1}{2} \rho v^2 + \frac{P}{\gamma - 1} + \frac{B^2}{8\pi} \right) + \nabla \cdot \left[ \left( \frac{1}{2} \rho v^2 + \frac{\gamma}{\gamma - 1} P \right. \right. \\ \left. \left. + \rho \Phi_{\text{tot}} \right) v + \frac{(\mathbf{B} \times \mathbf{v}) \times \mathbf{B}}{4\pi} \right] = -\rho \mathcal{L}, \end{aligned} \quad (3)$$

$$\frac{\partial \mathbf{B}}{\partial t} = \nabla \times (\mathbf{v} \times \mathbf{B}), \quad (4)$$

$$\nabla^2 \Phi = 4\pi G(\rho + \rho_{\text{sp}}). \quad (5)$$

Here,  $\rho$  is the gas density,  $\mathbf{v}$  is the gas velocity,  $P$  is the gas thermal pressure,  $\mathbf{B}$  is the magnetic field,  $\Phi_{\text{tot}} = \Phi + \Phi_{\text{ext}} + \Phi_{\text{tidal}}$  is the total gravitational potential,  $\rho \mathcal{L} = n_{\text{H}} [n_{\text{H}} \Lambda(T) - \Gamma]$  is the net cooling function,  $n_{\text{H}} = \rho / (\mu_{\text{H}} m_{\text{H}})$  is the number density of hydrogen nuclei, and all other symbols have their usual meaning. The quantity  $\rho_{\text{sp}}$  is the density of sink/star particles (representing stellar clusters formed by gravitational collapse) mapped onto the nearest  $3^3$  grid cells using the triangular-shaped-cloud scheme (Hockney & Eastwood 1981).

To follow radiative heating and cooling over the full range of temperatures and densities that occur in the three-phase ISM, a variety of approaches can be adopted. For most accurate treatment, time-dependent chemistry is required; although in general this is computationally quite expensive, it is also possible to design a reduced chemical network that retains just the most essential reactions for key coolants (e.g., Gong et al. 2017). For present purposes, we take the simpler approach of adopting a cooling coefficient  $\Lambda(T)$  using the fitting formula in Koyama & Inutsuka (2002, see Kim et al. 2008 for form with correction of typographical error) for  $T < 10^{4.2}$ , and collisional ionization equilibrium (CIE) cooling with solar metallicity from Sutherland & Dopita (1993) for  $T > 10^{4.2}$ . In order to obtain gas temperature from pressure and density, in principle we need to know the gas composition (or, in other words, the mean molecular weight,  $\mu$ ). However, here we do not follow detailed chemistry of molecule formation/dissociation and ionization/recombination. Instead, we simply use a tabulated mean molecular weight for the adopted CIE cooling at Solar metallicity of Sutherland & Dopita (1993). As temperature increases,  $\mu(T)$  varies from  $\mu_{\text{ato}} = 1.295$  for neutral gas (here we do not include molecular gas) to  $\mu_{\text{ion}} = 0.618$  for fully ionized gas. At intermediate temperatures,  $\mu$  is calculated iteratively for a given pair of  $P$  and  $\rho$ . The shape of the cooling function and mean molecular weight as a function of  $T$  are shown in Figure 1. For neutral gas, we include heating due to the photoelectric effect on grains; to exclude the ionized component we apply a normalization whose shape follows  $\mu(T)$  (see Equation (24)). The heating rate scales with the instantaneous FUV luminosity from sink/star particles (see Section 2.3.1 for details).

The external gravity in the vertical direction is modeled with a fixed potential. We use the Kuijken & Gilmore form (Kuijken & Gilmore 1989) with a modification for the dark matter potential at large  $|z|$ . The combined (old) stellar disk and dark

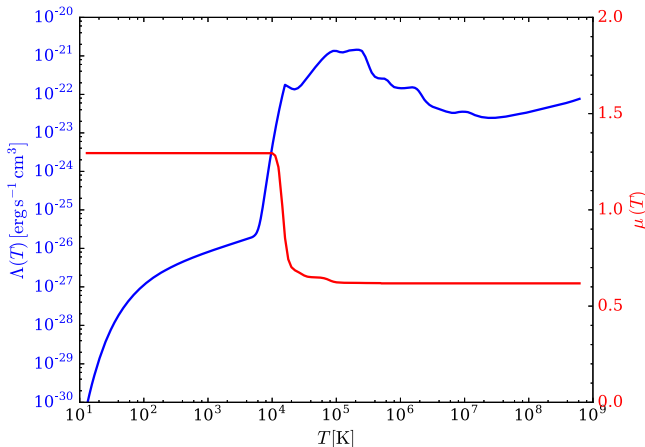


**Figure 1.** Left, blue: adopted cooling coefficient as a function of temperature, combining a fitting formula for the neutral ISM from Koyama & Inutsuka (2002) at  $T < 10^{4.2}$ , and CIE cooling from Sutherland & Dopita (1993) at  $T > 10^{4.2}$ . Right, red: adopted mean molecular weight as a function of temperature. We smoothly interpolate  $\mu$  between  $\mu_{\text{ato}} = 1.295$  and  $\mu_{\text{ion}} = 0.618$ , following the shape presented in Sutherland & Dopita (1993).

matter halo potential is given by

$$\Phi_{\text{ext}} \equiv 2\pi G \Sigma_* z_* \left[ \left( 1 + \frac{z^2}{z_*^2} \right)^{1/2} - 1 \right] + 2\pi G \rho_{\text{dm}} R_0^2 \ln \left( 1 + \frac{z^2}{R_0^2} \right). \quad (6)$$

Adopted parameters are given for the fiducial solar neighborhood model in Section 3. Alternative values of  $R_0$ ,  $\Sigma_*$ ,  $z_*$ , and  $\rho_{\text{dm}}$  can be adopted to represent other local environments, whether within the Milky Way or within other disk galaxies.

Our physics modules are implemented within the Athena code, which employs directionally unsplit Godunov methods to solve the ideal MHD equations, including the constrained-transport algorithm to preserve  $\nabla \cdot \mathbf{B} = 0$  (Stone et al. 2008). In this paper, we use Athena’s predictor-corrector type integrator (Stone & Gardiner 2009), adopting piecewise linear spatial reconstruction, and employing Roe’s Riemann solver. In addition, we apply “H-correction” (Sanders et al. 1998) when the difference in signal speed is larger than  $20 \text{ km s}^{-1}$  to suppress the carbuncle instability that can arise from strong blastwaves produced by SN explosions. We also apply “first-order-flux-correction” to cells with negative pressure and/or density after the second-order update; this situation can be produced by strong rarefaction waves in a highly turbulent medium (Lemaster & Stone 2009).

We solve Poisson’s equation (Equation (5)) using the FFT method with shearing-periodic boundary conditions in the horizontal directions (e.g., Gammie 2001) and vacuum boundary conditions in the vertical direction (Koyama & Ostriker 2009). The net cooling source term is solved fully implicitly in an operator-split manner before the integrator step. Because the cooling time  $t_{\text{cool}} \equiv |P|/[(\gamma - 1)\rho\mathcal{L}]$  in cold, dense gas is usually much shorter than the MHD time step,  $\Delta t$ , the cooling solver is sub-cycled if  $t_{\text{cool}} < \Delta t$ . For sub-cycling the cooling, we use an adaptive time step corresponding to the instantaneous cooling time. We neglect explicit thermal conduction, viscosity, and Ohmic resistivity. Other key features in the TIGRESS implementation are sink/star particles and

feedback in the form of stellar heating and SN explosions. We delineate the details of these below.

## 2.2. Sink/Star Particles

We use sink/star particles to trace formation and evolution of star clusters and to apply appropriate feedback from massive stars based on a population synthesis model. The original implementation of our sink particle method is described in Gong & Ostriker (2013, GO13). We modify this to accommodate a non-isothermal equation of state for sink creation, and to allow for non-accreting star particles (representing older clusters). We also implement a symplectic particle integration method for the shearing-box rotating frame, and introduce a particle age attribute needed to handle feedback from massive stars (the feedback itself is described in Section 2.3).

### 2.2.1. Sink Creation

We create a sink particle when the gas in a cell and its surroundings satisfies three conditions:

1. the density of the cell exceeds a threshold,
2. the cell is at the local potential minimum,
3. the flow is converging.

For the first condition, we use the Larson–Penston (Larson 1969; Penston 1969, LP) density threshold suggested by GO13,

$$\rho_{\text{thr}} \equiv \rho_{\text{LP}}(\Delta x/2) = \frac{8.86}{\pi} \frac{c_s^2}{G \Delta x^2}, \quad (7)$$

where  $c_s \equiv (P/\rho)^{1/2}$  is the sound speed of the cell. Note that the density threshold suggested by Truelove et al. (1997) has the same parameter dependence, but with a coefficient of  $\pi/16$  instead of  $8.86/\pi$ . As discussed by GO13, the motivations for using the LP density threshold are (1) the LP solution  $\rho_{\text{LP}}(r) \rightarrow 8.86c_s^2/(4\pi Gr^2)$  for  $r \rightarrow 0$  is an “attractor” of gravitational collapse, not just for the spherical case, but for arbitrary turbulent flows; and (2) the LP asymptotic solution guarantees supersonic collapse ( $v_r \rightarrow -3.28c_s$  for  $r \rightarrow 0$ ). For an isothermal equation of state, numerical simulations have validated that these two conditions hold quite generally in collapsing regions (e.g., Foster & Chevalier 1993; Vorobyov & Basu 2005; Gong & Ostriker 2011, 2015, and references therein). From the first condition, if the density reaches the threshold of Equation (7), it may be a signature that runaway gravitational collapse is occurring; the singularity implies that this collapse is inherently unresolved on a computational grid. The second condition is important because introduction of a sink particle could potentially alter the fluid variables in the surrounding volume if the inflow were subsonic; supersonic inflow ensures that the sink region is causally disconnected from its surroundings.

In order to check the validity of the LP approximation for a non-isothermal collapse, we have run collapsing simulations that include time-dependent heating and cooling. To set this up, we start with a spherical profile in which instantaneous thermal and dynamical equilibrium hold at each radius. This initial equilibrium profile can be uniquely determined by solving the static momentum equation, Poisson’s equation, and thermal equilibrium for the CNM branch, with given central

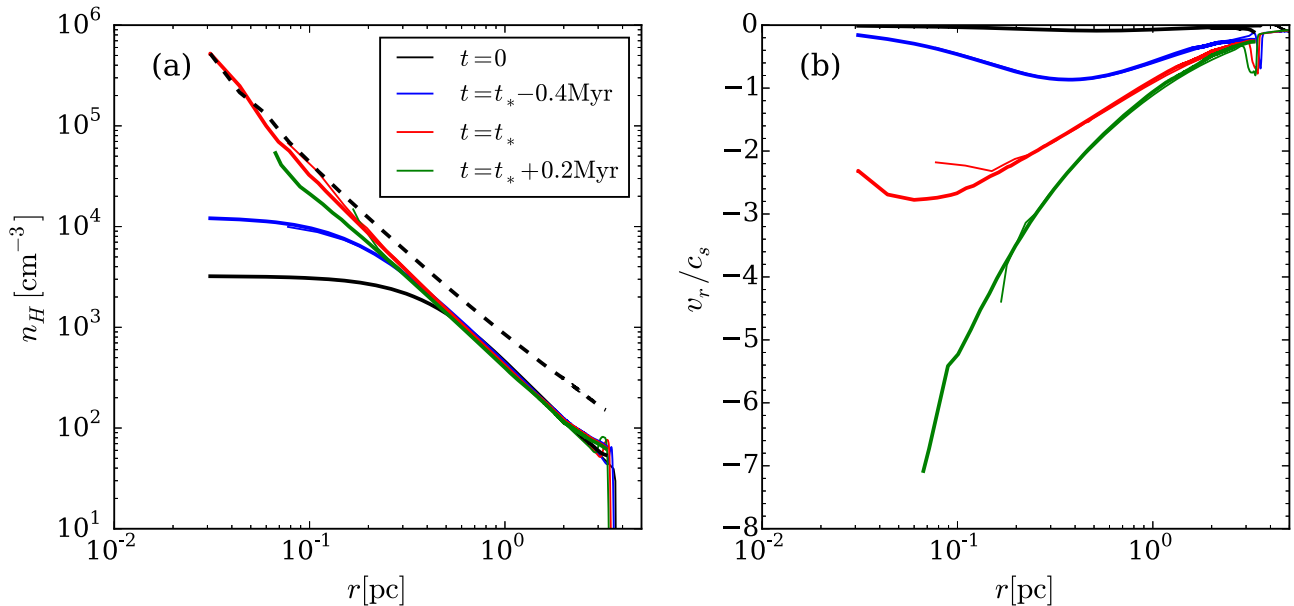


**Figure 2.** Collapse of non-isothermal sphere. Radial profiles of (a) number density and (b) radial Mach number  $v_r/c_s$  are shown for epochs of  $t = 0$  (initial condition; black),  $t = t_* - 0.4$  Myr (before singularity formation; blue),  $t = t_*$  (at the time of singularity formation; red), and  $t = t_* + 0.2$  Myr (after singularity formation; green). Thick and thin lines show high- ( $\Delta x = 0.031$  pc) and low-resolution ( $\Delta x = 0.078$  pc) runs, respectively. The dashed line in (a) denotes the LP density profile, with  $c_s(r)$  set by local values at the time of singularity formation.

temperature and edge pressure. Here, we use  $T_{\text{center}} = 20$  K and  $P_{\text{edge}}/k_B = 2000 \text{ cm}^{-3}$  K. To initiate collapse, we multiply the density and pressure by a factor of 2. Due to the short cooling time, the temperature immediately readjusts to restore thermal equilibrium, but gravity is not balanced by pressure and the sphere undergoes collapse similar to that of an isothermal sphere.

Figure 2 plots (a) number density and (b) radial Mach number  $v_r/c_s$  as a function of radius for several different times. The initial condition is shown in black; profiles before (blue), at (red), and after singularity formation (green) are also shown. The dashed line in (a) denotes the LP density profile,  $\rho_{\text{LP}} = 8.86c_s^2(r)/(4\pi Gr^2)$  with sound speed at each radius set by local values at the time of singularity. Because  $c_s$  is not a constant but increases outward, this density profile is slightly shallower than that in the isothermal case  $\rho_{\text{LP}} \propto r^{-2}$ . The collapse starts from large radius and propagates inward (i.e., the location of the velocity extremum moves inward; e.g., Gong & Ostriker 2009). Eventually, the radial collapsing velocity exceeds the local sound speed, and the density profile of the inner part approaches the dashed line. When the central density reaches the LP density threshold (Equation (7) using the local  $c_s$ ), we create a sink particle, and continue to follow the late-time accretion. At the time of singularity formation,  $v_r \sim -3c_s$  for the high-resolution run. If we do not create a sink particle when the central density reaches the LP threshold, unresolved collapse causes unphysical overshoots of density and out-of-equilibrium temperature; this failure is why sink particles are required. Figure 2 shows that, when we apply the LP density threshold as the creation criterion for sink particles, unphysical behavior does not arise and both low- and high-resolution runs give essentially the same density and velocity profiles before, at, and after singularity formation.

Because cold gas where collapse occurs is generally quite close to thermal equilibrium, we can estimate typical values of the LP threshold density for given  $\Delta x$  and cooling/heating functions. For the CNM ( $T < 200$  K), the cooling function can be approximated

by  $\Lambda(T) \approx 2.8 \times 10^{-28}\sqrt{T} \exp(-92/T)$  erg s<sup>-1</sup>cm<sup>3</sup>, where  $T$  is the temperature in Kelvins. The thermal equilibrium condition ( $n_{\text{H}}\Lambda(T) - \Gamma = 0$ ) can then be solved for the equilibrium density at a given temperature. By equating the thermal equilibrium density to  $n_{\text{thr}} = \rho_{\text{thr}}/(\mu_{\text{H}}m_{\text{H}}) \propto T/(\Delta x)^2$ , the threshold temperature ( $T_{\text{thr}}$ ) is given by the nonlinear equation

$$T_{\text{thr}}^{3/2} \exp\left(-\frac{92}{T_{\text{thr}}}\right) = 0.6 \left(\frac{\Gamma}{\Gamma_0}\right) \left(\frac{\Delta x}{\text{pc}}\right)^2, \quad (8)$$

where  $\Gamma_0 = 2 \times 10^{-26}$  erg s<sup>-1</sup> is adopted for the solar neighborhood (see Koyama & Inutsuka 2002). Given the solution  $T_{\text{thr}}$ , the sink particle density threshold using the LP condition is then obtained from Equation (7). The corresponding density threshold from the Truelove condition would use a coefficient of  $\pi/16$  instead of  $8.86/\pi$ .

Figure 3 shows the threshold density, temperature, and pressure that satisfy both the LP density threshold and thermal equilibrium, as a function of  $\Delta x$  for  $\Gamma = \Gamma_0$ . We overplot (as dotted lines) the maximum equilibrium temperature of the CNM (184 K, blue) and the two-phase pressure ( $P_{\text{two}} = 3110k_B \text{ cm}^{-3} \text{ K}(\Gamma/\Gamma_0)$ , red) defined by the harmonic mean of the maximum and minimum equilibrium pressures of the WNM and CNM, respectively. Here,  $P_{\text{two}}$  is characteristic of the midplane thermal pressure in the warm/cold atomic ISM when star formation is in a self-regulated state (Ostriker et al. 2010; Kim et al. 2011, 2013). Note that these particular values of  $T_{\text{CNM, max}}$  and  $P_{\text{two}}$  depend on the adopted cooling curve and on the value of  $\Gamma$ .

For self-gravitating collapse to be numerically captured under typical ISM conditions, the central pressure of a collapsing cloud at the local simulation resolution must be sufficiently high compared to the typical ambient ISM pressure; i.e.,  $P_{\text{thr}}$  must be large enough compared to  $P_{\text{two}}$ . If the resolution is too low, collapse cannot be captured. For example, Figure 3 shows that resolution  $\Delta x < 20$  pc would be needed

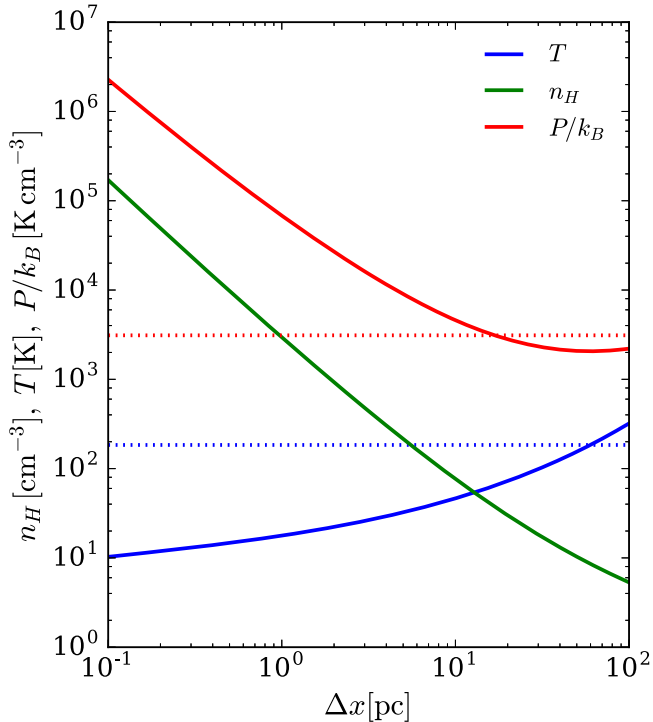


**Figure 3.** Estimated threshold density, temperature, and pressure for sink particle creation as a function of spatial resolution  $\Delta x$ . Solid lines show the threshold conditions defined by simultaneous satisfaction of thermal equilibrium and the LP density threshold condition (Equation (7)). The horizontal dotted lines denote the maximum equilibrium temperature of the CNM ( $=184 \text{ K}$ , blue) and the two-phase pressure ( $P_{\text{two}} = 3110 k_B \text{ cm}^{-3} \text{ K}(\Gamma/\Gamma_0)$ , red). At high resolution, the threshold pressure is well above  $P_{\text{two}}$ .

for the expected central pressure of a collapsing cloud to exceed that of the environment under solar-neighborhood conditions ( $\Gamma = \Gamma_0$ ). We note that the resolution needed to obtain  $P_{\text{thr}} \gg P_{\text{two}}$  and capture collapse is easily accessible for local simulations, but that even the marginal resolution needed for  $P_{\text{thr}} \sim P_{\text{two}}$  is inaccessible for current cosmological galaxy formation simulations.

After identifying any location where the threshold density is exceeded, we check the second two criteria for sink particle formation. In particular, we first test whether the gravitational potential in a candidate cell is the minimum in the control volume of the  $3^3$  surrounding cells. Finally, we check flow convergence in all directions,  $dv_x/dx < 0$ ,  $dv_y/dy < 0$ , and  $dv_z/dz < 0$  (not simply  $\nabla \cdot \mathbf{v} < 0$ ). We note that, if the resolution is high enough, the additional criteria are essentially always satisfied (see GO13). The control volume has an effective radius of  $r_{\text{ctrl}} \equiv 1.5 \Delta x$ , and we check whether there are any existing sink particles within  $2r_{\text{ctrl}}$ . If there are, a new sink particle will not be created.

For a cell that passes all the above conditions, we create a sink particle at the cell center. When a sink particle is created, the control volume is treated as ghost zones for the purpose of resetting the fluid variables. For example, the cells at faces, sides, and corners of the cubic control volume use averages of (respectively) one, two, and three contact cells in the surrounding grid to compute the density, momentum, and pressure. The cell containing the sink particle uses the average of six contact cells to compute its density, momentum, and pressure. In the shearing box, we need to carefully subtract and add the background velocity for corresponding cells, before

taking and after applying averages, respectively. Note that we do not reset magnetic fields in the control volume. After the control volume density and momentum are reset as ghost zones, the sink particle mass and velocity are assigned such that the total mass and momentum of sink particle + control volume are equal to the value integrated over all  $3^3$  zones prior to sink particle creation.

Finally, we note that we immediately treat a sink particle as a star cluster. This implicitly assumes that the “star formation timescale”—representing the interval from the beginning of gravitational collapse to star cluster formation—is negligible compared to other relevant timescales. In particular, our treatment is valid provided that the “feedback timescale”—the interval between star cluster formation and the first SN event ( $\sim 4$  Myr for STARBURST99)—is longer than “the star formation timescale.” Physically, it is reasonable to assume that massive stars would form within a free-fall time at the threshold density. In this light, instantaneous introduction of a sink particle would be valid up to resolution of  $\Delta x = 8 \text{ pc}$ , where  $n_{\text{thr}} \gtrsim 100 \text{ cm}^{-3}$  and  $t_{\text{ff}} \sim 4 \text{ Myr}$ . In low-resolution models with lower  $n_{\text{thr}}$ , the free-fall time would exceed the true time before the onset of feedback. However, we do not explicitly introduce a time delay to account for this. Also, low resolution tends to lead to very massive sink particles, whereas in a higher-resolution simulation, there would have been several smaller sinks that form at different times. Taken together, these effects tend to (unphysically) increase the spacetime correlation of star formation and feedback at low resolution, as we shall show later.

## 2.2.2. Sink Accretion and Merging

In contrast to the original GO13 implementation, subsequent to particle creation, we reset control volume fluid variables and add mass and momentum to sink particles only when gas is converging to the control volume in all three directions. This modification is desirable because the current simulations develop very strong turbulence, such that there can be large relative velocities of particles and the surrounding gas. To check for flow convergence, we define the right/left face-averaged fluxes in the sink particle’s reference frame as

$$\bar{\mathcal{F}}_{r/l} \equiv \sum_{j,k} \mathcal{F}_{\rho,i+2/i-1,j,k} \left( 1 - v_{x,\text{sp}} \frac{\mathcal{F}_{\rho,i+2/i-1,j,k}}{\mathcal{F}_{\rho v_x,i+2/i-1,j,k}} \right), \quad (9)$$

$$\bar{\mathcal{G}}_{r/l} \equiv \sum_{i,k} \mathcal{G}_{\rho,i,j+2/j-1,k} \left( 1 - v_{y,\text{sp}} \frac{\mathcal{G}_{\rho,i,j+2/j-1,k}}{\mathcal{G}_{\rho v_y,i,j+2/j-1,k}} \right), \quad (10)$$

$$\bar{\mathcal{H}}_{r/l} \equiv \sum_{i,j} \mathcal{H}_{\rho,i,j,k+2/k-1} \left( 1 - v_{z,\text{sp}} \frac{\mathcal{H}_{\rho,i,j,k+2/k-1}}{\mathcal{H}_{\rho v_z,i,j,k+2/k-1}} \right), \quad (11)$$

where  $\mathcal{F}$ ,  $\mathcal{G}$ , and  $\mathcal{H}$  stand for fluxes in the  $x$ -,  $y$ -, and  $z$ -directions defined at cell faces, respectively, and  $i$ ,  $j$ , and  $k$  in the summation run from  $i-1$  to  $i+1$ ,  $j-1$  to  $j+1$ , and  $k-1$  to  $k+1$ , respectively, for a particle in a cell at  $(i, j, k)$ . We check the converging flow condition using  $\bar{\mathcal{F}}_r < 0$  and  $\bar{\mathcal{F}}_l > 0$ , or equivalently,  $\bar{\mathcal{F}}_r - \bar{\mathcal{F}}_l < 0$  and  $\bar{\mathcal{F}}_r \bar{\mathcal{F}}_l < 0$ , and similarly for  $\bar{\mathcal{G}}$  and  $\bar{\mathcal{H}}$ . Note that these fluxes are calculated at  $t^{n+1/2}$ , so we also need to know particles’ velocity at this time, which is what the particle integrator returns (see Section 2.2.5).

When the converging-flow condition is satisfied, the particle accretes mass and momentum as in GO13. The accretion rates

of mass and momentum to each sink particle are calculated based on the fluxes returned by the Riemann solver at the control volume boundary, combined with the mass and momentum differences within the control volume between the new, step  $(n + 1)$ , and old, step  $n$ , control volumes if sink particles move across grid zones (see GO13). In order to calculate the accretion rate due to particles' movement, we need to advance sink particles' positions before the MHD integrator step, where we calculate the accretion rate based on the fluxes. This is important in preserving Galilean invariance of particle accretion (see test problem in Section 3.3 of GO13). Note that accretion can occur for a given particle before it hosts its first SN event (see Section 2.3); after this time, sink particles become star particles and cease to accrete.

When the distance between two sink particles is smaller than  $2r_{\text{ctrl}}$ , we merge them by creating a new sink particle at the center of mass of the two. All properties for the new sink particle are set by mass-weighted averages.

### 2.2.3. Sink/Star Particle Types

We separate sink/star particles into three categories based on their (mean) age  $t_m$ .

1. “Growing” particles:  $0 < t_m < t_{\text{SN}}$ . This group consists of particles between their birth and their first SN event. The mean SN onset time is  $t_{\text{SN}} \sim 4$  Myr, but for any sink/star particle, individual SN events are determined stochastically based on the rate from STARBURST99 (see Figure 5). “Growing” particles are treated as sinks; as described above, they can accrete gas and merge with other “growing” particles. They exert gravity and contribute to the total mean FUV radiation.
2. “Feedback” particles:  $t_{\text{SN}} < t_m < t_{\text{life}}$ . This group consists of star particles between their first SN event and the adopted feedback lifetime  $t_{\text{life}} \equiv 40$  Myr. These particles do not accrete and merge; their motion is simply integrated as in Section 2.2.5. These particles exert gravity by contributing to  $\rho_{\text{sp}}$ , and contribute total mean FUV radiation (Section 2.3.1) and SN feedback (Section 2.3.2).
3. “Passive” particles:  $t_{\text{life}} < t_m$ . This group of particles is no longer active, and affects the gas and other particles only through the gravity they exert.

In addition, we use “runaway” particles to follow the position of runaways (see Section 2.3.2). These particles are massless “passive” particles and have no effect on the gravity or gas. They are ejected from sink/star particles and host one SN event after an assigned delay time  $\tau_{\text{run}}$ .

### 2.2.4. Sink/Star Aging

After their formation, sink/star particles must age in time in order for feedback to be appropriately applied based on the stellar population of the clusters they represent. To represent birth of a young stellar population from newly accreted gas, we assign individual sink/star particles a mass-weighted mean age:

$$t_m = \frac{m_{\text{sp}}(t_m + \Delta t) + \Delta m \Delta t}{m_{\text{sp}} + \Delta m}, \quad (12)$$

where  $\Delta m$  is the mass increment during a hydrodynamic time step  $\Delta t$ . Note that simple aging  $t_m = t_m + \Delta t$  is recovered as

$\Delta m \rightarrow 0$ . When two particles merge, the age is also calculated by taking a mass-weighted mean.

### 2.2.5. Particle Motion Integration

We integrate particles' positions and velocities from the equation of motion in a shearing box with gravity from both gas and particles, as well as the fixed gravitational potential from the old stellar disk. Since self-gravity is evaluated at steps  $n$  and  $n + 1$ , not at  $n + 1/2$ , it is advantageous to use a “Kick-Drift-Kick (DKK)” form of a leap-frog integrator. The general form of a DKK integrator can be written as

$$\mathbf{v}^{n+1/2} = \mathbf{v}^{n-1/2} + \mathbf{a}(\mathbf{x}^n, \mathbf{v}) \Delta t, \quad (13)$$

$$\mathbf{x}^{n+1} = \mathbf{x}^n + \mathbf{v}^{n+1/2} \Delta t. \quad (14)$$

The acceleration  $\mathbf{a}$  is the same as in the right-hand side of Equation (2) divided by  $\rho$ . It consists of the effective gravity,  $-\nabla\Phi_{\text{tot}}$ , which depends on position, and the Coriolis force,  $-2\Omega \times \mathbf{v}$ , which depends on velocity. Depending on the choice of velocity in the acceleration term, one can write down KDK integrators in explicit  $\mathbf{v} \equiv \mathbf{v}^{n-1/2}$ , implicit  $\mathbf{v} \equiv \mathbf{v}^{n+1/2}$ , and semi-implicit  $\mathbf{v} \equiv (\mathbf{v}^{n-1/2} + \mathbf{v}^{n+1/2})/2$  forms (see Bai & Stone 2010 for DKD integrators). However, those integrators are not symplectic in a shearing box.

Here, we adopt a symplectic integrator for Hill's equation suggested by Quinn et al. (2010, Q10) with a generalization for an arbitrary rotation profile with shear parameter  $q \equiv -d \ln \Omega / d \ln R$ . The full set of equations to advance velocity and position of a particle from  $t^n$  to  $t^{n+1}$  is as follows.

#### 1. First Kick:

$$v_x^{n+1/2} = v_x^n + h f_x^n + 2h\Omega(P_y^n - 2\Omega x^n) \quad (15)$$

$$v_y^{n+1/2} = P_y^n - 2\Omega x^n - 2h\Omega v_x^{n+1/2} \quad (16)$$

$$v_z^{n+1/2} = v_z^n + h f_z^n, \quad (17)$$

where  $h \equiv \Delta t/2$ ,  $P_y^n \equiv v_y^n + h f_y^n + 2\Omega x^n$ , and  $f = -\nabla\Phi_{\text{tot}}^n$ ;

#### 2. Full Drift:

$$\mathbf{x}^{n+1} = \mathbf{x}^n + \mathbf{v}^{n+1/2} \Delta t; \quad (18)$$

#### 3. Second Kick:

$$v_x^{n+1} = v_x^{n+1/2} + h f_x^{n+1} + 2h\Omega(P_y^n - 2\Omega x^{n+1}) \quad (19)$$

$$v_y^{n+1} = P_y^n - 2\Omega x^{n+1} + h f_y^{n+1} \quad (20)$$

$$v_z^{n+1} = v_z^{n+1/2} + h f_z^{n+1}. \quad (21)$$

In practice, the self-gravity that enters in the second kick step (through  $f^{n+1}$ ) is not available until time  $t^{n+1}$  because it requires an update of the gas density by the MHD integrator. Thus, while the position can be fully drifted to  $t^{n+1}$ , the velocity can be kicked only to  $t^{n+1/2}$ . This means that  $v_x^n$  and  $v_y^n$  appearing in Equations (15) and (16) are not immediately available. We therefore must begin each step by applying the “second kick” to the velocity associated with the previous timestep; i.e., for step  $n'$ , we would apply Equations (19)–(21) with  $n = n' - 1$ , which make use of  $f^{n'}$ . Having particle velocities at  $t^{n+1/2}$  is also useful for computing mass fluxes for evaluating the accretion onto sink particles.

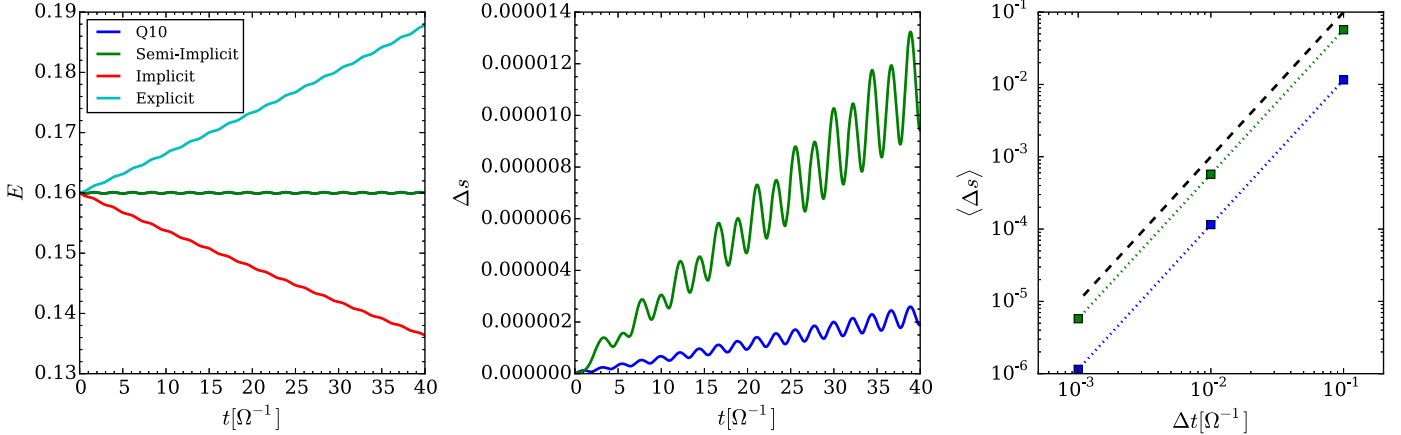


**Figure 4.** Results of epicyclic motion tests for our adopted symplectic integrator (Q10; shown in all panels in blue), in comparison to explicit (cyan; left panel), semi-implicit (green; all panels), and implicit (red; left panel) KDK integrators. Left and middle panels, respectively, show time evolution of energy ( $E$ ) and position offset ( $\Delta s$ ) of the orbit for  $\Delta t = 10^{-3} \Omega$ . Right panel shows convergence of the mean  $\langle \Delta s \rangle$  as a function of time step. The dashed line in the right panel shows second order convergence.

We test our particle integrator using epicyclic orbits. With only the gravitational force that produces the background rotation curve of the galaxy ( $\Phi_{\text{tot}} = \Phi_{\text{tidal}}$ ), a particle’s motion in a shearing box follows a planar epicyclic orbit described by

$$x(t) = A \cos(\kappa t), \quad y(t) = \frac{2\Omega}{\kappa} A \sin(\kappa t), \quad (22)$$

where  $\kappa \equiv \sqrt{2(2 - q)} \Omega$  is the epicyclic frequency and  $A$  is the (arbitrary) amplitude of the orbit. For this test, we adopt  $(A, q, \Omega) \equiv (0.4, 1, 1)$ , which gives the total energy of the orbit,

$$E = \frac{1}{2}(\dot{x}^2 + \dot{y}^2) + \Phi_{\text{tidal}} = (2 - q)\Omega^2 A^2 = 0.16. \quad (23)$$

Figure 4 shows energy (left) and position offset (middle) of the orbit for  $\Delta t = 10^{-3}/\Omega$ , and convergence of position offset as a function of time step (right). For comparison, we also present results from explicit, semi-implicit, and implicit KDK integrators. Both the semi-implicit and Q10 methods show good energy conservation, without the secular energy increase of the explicit integrator or decrease of the implicit integrator. Position offsets (consisting of a phase shift, but not a change in the semimajor axis) increase over time for both semi-implicit and Q10 methods, with the Q10 integrator giving better results and more regular fluctuation. The mean phase errors over  $t\Omega = 40$  (right panel) show second-order convergence as the time step gets smaller. For our fiducial model with  $\Delta x = 4$  pc, typical timesteps have  $\Omega\Delta t \sim 10^{-4}\text{--}10^{-5}$ .

### 2.3. Star Formation Feedback

#### 2.3.1. FUV Radiation and Photoelectric Heating

For warm and cold gas, we implement photoelectric heating on grains. In reality, the heating rate at any location in the ISM depends on the dust density (which we assume is simply proportional to the gas density) and the angle-averaged FUV intensity  $J_{\text{FUV}}$ . In the present implementation, we do not attempt direct radiative transfer from the active sink/star particles to compute  $J_{\text{FUV}}$  at every spatial location (see note below), but we do vary the heating rate temporally, based on the mean FUV radiation that the massive young stellar population would produce at any time. For a sink/star particle

with mass  $m_{\text{sp}}$  and mass-weighted mean age  $t_{\text{m}}$ , the FUV luminosity is  $L_{\text{FUV,sp}} = \Psi_{\text{FUV}}(t_{\text{m}})m_{\text{sp}}$ . Here, we use a tabulated luminosity-to-mass ratio,  $\Psi_{\text{FUV}}(t)$ , for FUV radiation ( $6 \text{ eV} < h\nu < 13.6 \text{ eV}$ ) from STARBURST99 with a fully sampled Kroupa IMF (Kroupa 2001; see blue solid line and left axis in Figure 5).

We calculate total FUV luminosity  $L_{\text{FUV}}$  by summing  $L_{\text{FUV,sp}}$  from all sink/star particles. We further assume that  $4\pi J_{\text{FUV}} \propto \Sigma_{\text{FUV}} \equiv L_{\text{FUV}}/(L_x L_y)$ , where for the optically thin case and a uniform source distribution at the midplane, equality would hold.<sup>1</sup> We compute the contribution to the photoelectric heating rate from the local disk assuming  $\Gamma \propto J_{\text{FUV}}$ , where  $\Sigma_{\text{FUV},0} = 6.9L_{\odot}/\text{pc}^2$ , corresponding to  $J_{\text{FUV},0} = 2.2 \times 10^{-4} \text{ erg s}^{-1} \text{ cm}^{-2} \text{ sr}^{-1}$  (or  $G_0 = 1.7$  in Habing units; Draine 1978), yields  $\Gamma_0 = 2 \times 10^{-26} \text{ erg s}^{-1}$ .

Including the temperature dependence of the mean molecular weight (to turn off photoelectric heating at high temperature) and adding a heating floor due to the metagalactic FUV ( $4\pi J_{\text{FUV,meta}} = 6.7 \times 10^{-6} \text{ erg s}^{-1} \text{ cm}^{-2}$  or  $J_{\text{FUV,meta}}/J_{\text{FUV},0} = 0.0024$ ; Sternberg et al. 2002), the adopted heating rate becomes

$$\Gamma = \Gamma_0 \left( \frac{\mu(T) - \mu_{\text{ion}}}{\mu_{\text{ato}} - \mu_{\text{ion}}} \right) \left( \frac{\Sigma_{\text{FUV}}}{\Sigma_{\text{FUV},0}} + 0.0024 \right). \quad (24)$$

Both “growing” and “feedback” sink/star particles contribute to the FUV luminosity.

#### 2.3.2. Supernova Rates and Runaways

Let  $\xi_{\text{SN}}(t_{\text{m}}) \equiv d(\mathcal{N}_{\text{SN}}/M_{\text{cl}})/dt$  be the specific SN rate, defined as the number of SNe per unit time per star cluster mass for a cluster of mean age in the interval  $(t_{\text{m}}, t_{\text{m}} + dt)$ . We adopt results for  $\xi_{\text{SN}}$  tabulated from STARBURST99 (Leitherer

<sup>1</sup> The mean FUV intensity,  $J_{\text{FUV}}$ , should be obtained by full radiation transfer. Although computationally expensive, time-dependent transfer can be incorporated with ray-tracing methods, provided that the number of active sources is not too large; implementation of this is underway. For present purposes, we note (Ostriker et al. 2010) that simple slab geometry of gas with UV optical depth of  $\tau_{\perp} = \kappa\Sigma$  gives  $4\pi J_{\text{FUV}} = \Sigma_{\text{FUV}}(1 - E_2(\tau_{\perp}/2))/\tau_{\perp}$ , where  $E_2$  is the second exponential integral. For  $\tau_{\perp} \sim 0.1\text{--}1$ , the correction term varies from  $\sim 1.7$  to  $0.7$ . Therefore,  $4\pi J_{\text{FUV}} \approx \Sigma_{\text{FUV}}$  is a valid assumption to zeroth order. In forthcoming work, we will investigate the distribution of FUV radiation for simulation snapshots of gas- and star-particle source distributions.

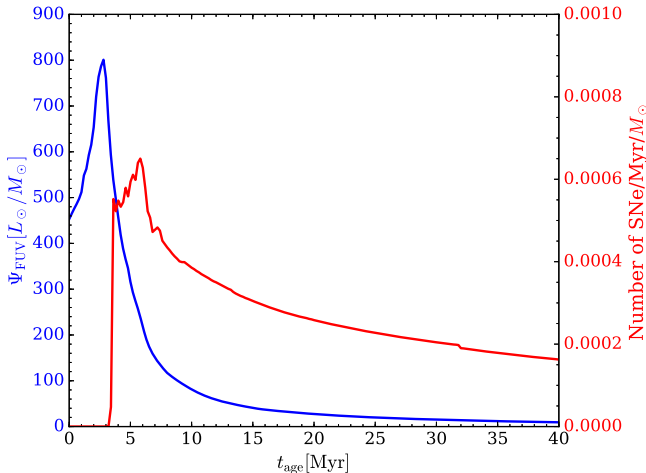


**Figure 5.** Left axis, blue: specific FUV luminosity of star clusters ( $\Psi_{\text{FUV}} \equiv L_{\text{FUV}}/M_{\text{cl}}$ ) as a function of cluster age, assuming a fully sampled Kroupa IMF. Right axis, red: specific SN rate of star clusters ( $\xi_{\text{SN}} \equiv d(N_{\text{SN}}/M_{\text{cl}})/dt$ ) as a function of cluster age.

et al. 1999) for a fully sampled Kroupa IMF (see red solid line and right axis in Figure 5). This gives a total mass of new stars per SN,  $m_*$ ,

$$m_* \equiv \left( \int_0^{t_{\text{life}}} \xi_{\text{SN}} dt \right)^{-1} = 95.5 M_\odot. \quad (25)$$

For a sink/star particle with mass  $m_{\text{sp}}$  and mass-weighted mean age  $t_m$ , the expected number of SNe during the MHD time step  $\Delta t$  is  $N_{\text{SN}} = m_{\text{sp}} \xi_{\text{SN}}(t_m) \Delta t$ . In the simulation, we sample a random number  $\mathcal{U}_{\text{SN}}$  in (0,1) and a SN event occurs if  $N_{\text{SN}} > \mathcal{U}_{\text{SN}}$ . The mean value of  $\xi_{\text{SN}}$  over the lifetime of a sink/star particle is  $\langle \xi_{\text{SN}} \rangle = (m_* t_{\text{life}})^{-1}$  and the SN rate varies by only a factor  $\sim 3$ , so typically  $N_{\text{SN}} \sim m_{\text{sp}} \Delta t / (m_* t_{\text{life}})$ . Note that if  $N_{\text{SN}} > 1$ , more than one SN would be expected in a single epoch. However, considering our typical timestep,  $\Delta t \sim 10^{-3}\text{--}10^{-5}$  Myr, and sink/star particle mass,  $m_{\text{sp}} = 10^3\text{--}10^5 M_\odot$ , this never happens in practice.

We include runaway OB stars to represent SN events that occur far from star clusters.<sup>2</sup> Runaways may occur because of (1) dynamical interactions during the birth of a star cluster (e.g., Poveda et al. 1967; Fujii & Portegies Zwart 2011; Oh et al. 2015) and (2) SNe in OB binary systems (e.g., Blaauw 1961; Portegies Zwart 2000; Eldridge et al. 2011). In the current TIGRESS implementation, our treatment of runaways is based on the second mechanism. Whenever there is a SN event ( $N_{\text{SN}} > \mathcal{U}_{\text{SN}}$ ), we additionally check whether this event occurs in a single star or a binary system for a given binary fraction of OB stars  $f_{\text{bin}}$  (2/3 is our standard choice). Here, this binary fraction is defined as

$$\begin{aligned} f_{\text{bin}} &\equiv \frac{\text{Number of OB stars in binaries}}{\text{Number of total OB stars}} \\ &\equiv \frac{N_{\text{bin}}}{N_{\text{tot}}} = \frac{N_{\text{bin,p}} + N_{\text{bin,s}}}{N_{\text{single}} + N_{\text{bin}}}, \end{aligned} \quad (26)$$

where the number of primaries and secondaries is  $N_{\text{bin,p}} = N_{\text{bin,s}} = N_{\text{bin}}/2$ . If the event is not in a binary, we simply assign

<sup>2</sup> Note that, in this work, we neglect Type Ia SNe, whose rates are typically 10–20% of the SNe rate from massive stars (e.g., Tammann et al. 1994). However, runaway SNe capture the most important effect of Type Ia SNe, namely a broad spatial distribution of SN events far from young star clusters.

an SN event at the sink/star particle position following Section 2.3.3.

If the event is defined as an SN in a binary, we allow for both an immediate in situ primary SN explosion and a runaway secondary that produces a SN explosion after a time delay. Runaways are massless star particles ejected isotropically with initial velocity distribution consistent with a binary population synthesis model (Figure 2 of Eldridge et al. 2011). Each runaway is a time bomb with a delay time  $\tau_{\text{run}}$ . In order to have the overall SN rate consistent with  $\xi_{\text{SN}} m_{\text{sp}}$ , we set the delay time using the probability integral transform,  $\tau_{\text{run}} = \Xi_{\text{SN}}^{\text{inv}}(\mathcal{U}_{\text{run}})$ , where  $\mathcal{U}_{\text{run}}$  is another uniform random number in (0,1), the normalized cumulative distribution of SNe is

$$\Xi_{\text{SN}}(t) \equiv \frac{\int_0^t \xi_{\text{SN}} dt}{\int_0^{t_{\text{life}}} \xi_{\text{SN}} dt} = \int_0^t \xi_{\text{SN}} m_* dt, \quad (27)$$

and  $\Xi_{\text{SN}}^{\text{inv}}$  is the inverse function of  $\Xi_{\text{SN}}$ . We tabulate  $\Xi_{\text{SN}}$  from the tabulated  $\xi_{\text{SN}}$ . Once we obtain  $\tau_{\text{run}}$ , we compare it with  $t_m$ . When  $\tau_{\text{run}} > t_m$ , a massless star particle is ejected and will be exploded after  $\tau_{\text{run}}$ . We also explode an SN at the original sink/star particle position, representing the explosion of the primary. Otherwise (if  $\tau_{\text{run}} < t_m$ ), we simply do nothing for this unphysical situation (causality violation).

### 2.3.3. Supernova Feedback Treatment

For any SN event, we first determine the feedback prescription that is applied. We use three types of feedback in TIGRESS: EJ (Ejecta), ST (Sedov–Taylor), and MC (Momentum Conserving). Our goals in defining and selecting from among these prescriptions are to assign thermal energy and momentum appropriate for the resolution of the simulation and local properties of the ambient environment, avoiding both numerical “overcooling” and a subsequent time step that is very small. In the ST and EJ feedback prescriptions, we reset density, momenta, and thermal energy within a sphere of radius  $R_{\text{snr}}$ . In the MC feedback prescription, the thermal energy and density are unchanged, but velocities are reset within  $R_{\text{snr}}$ . Magnetic fields remain unchanged.

To choose which prescription is applied, we calculate the mean gas properties in cells surrounding the SN with  $d_{ijk} < R_{\text{snr}}$ , where  $d_{ijk}$  is the distance of a cell from the SN. We vary  $R_{\text{snr}}$  starting from  $R_{\text{snr,min}} = 3\Delta x$  to  $R_{\text{snr,max}}$  (the choice of  $R_{\text{snr,max}}$  is model-dependent) with an increment of  $\Delta R = \Delta x/2$ . For every  $R_{\text{snr}}$ , we first calculate the total mass within the initial “SN remnant,”  $M_{\text{snr}} \equiv \sum \rho_{ijk} (d_{ijk} < R_{\text{snr}}) \Delta V + M_{\text{ej}}$ , and the mean density  $\rho_{\text{snr}} \equiv M_{\text{snr}} / \sum_{d_{ijk} < R_{\text{snr}}} \Delta V$ , where  $M_{\text{ej}} = 10 M_\odot$  represents the mass of ejecta plus circumstellar medium. We then calculate the ratio of the initial remnant mass to the expected shell formation mass,  $\mathcal{R}_M \equiv M_{\text{snr}} / M_{\text{sf}}$ , where  $M_{\text{sf}} = 1679 M_\odot (n_{\text{H}} / \text{cm}^{-3})^{-0.26}$  can be estimated from numerical simulations of individual expanding SNR with ambient density  $n_{\text{H}}$  that include cooling (e.g., Kim & Ostriker 2015a, KO15a). Here, we use the mean molecular weight per hydrogen atom  $\mu_{\text{H}} \equiv 1.427$  to obtain the hydrogen number density  $n_{\text{H}} = \rho_{\text{snr}} / (\mu_{\text{H}} m_{\text{H}})$ . Shell formation occurs when post-shock gas at the forward shock of an expanding SN remnant first becomes strongly radiative.

If  $\mathcal{R}_M > 1$  for  $R_{\text{snr,min}}$ , the Sedov–Taylor stage of this SN is unresolved. This case occurs if resolution is low and/or local density is high, and the SN remnant would become

radiative at a scale smaller than that is locally resolved. In this case, our treatment of feedback just injects momentum to the grid using the final radial momentum  $p_{\text{snr}} = 2.8 \times 10^5 M_\odot \text{ km s}^{-1} (n_{\text{H}} / \text{cm}^{-3})^{-0.17}$  computed from resolved numerical simulations of a single SN in a two-phase medium (see KO15a); other resolved simulations for an inhomogeneous medium find similar final momenta (Martizzi et al. 2015; Iffrig & Hennebelle 2015; Walch & Naab 2015). We refer to this type of feedback as MC, as momentum is assumed to be conserved from the unresolved scale at which the remnant would cool to the resolved scale at which momentum is injected to the grid.

If  $0.027 < \mathcal{R}_M < 1$  for given  $R_{\text{snr}}$ , we assign total SN energy  $E_{\text{SN}} = 10^{51} \text{ erg}$  in both thermal and kinetic forms to the gas within the feedback region,  $d_{ijk} < R_{\text{snr}}$ . The energy ratio is appropriate for the energy conserving phase ( $\sim 72\%$  in thermal, and  $\sim 28\%$  in kinetic). We refer to this type of feedback as ST, as it represents a remnant that is in the Sedov–Taylor stage.

Note that, as long as  $\mathcal{R}_M < 1$  and the ambient medium is uniform, KO15a showed that SNRs are sufficiently resolved that either the ST or pure thermal energy prescription (dumping the total SN energy to thermal energy) will provide correct feedback. However,  $\mathcal{R}_M \sim 1$  (or  $\Delta x/r_{\text{sf}} \sim 1/3$ ) is marginal. Thus, if the density were *not* uniform within  $R_{\text{snr}}$ , the gas at higher-than-average density would cool faster. Equivalently, the value of  $M_{\text{sf}}(n_{\text{H}})$  evaluated using  $n_{\text{H}}$  from the overdense portions of the feedback region would be lower than if the mean density were used, and the corresponding  $\mathcal{R}_M$  would exceed unity. Therefore, if a thermal dump were applied to *inhomogeneous* gas with  $\mathcal{R}_M \sim 1$ , it would lead to “overcooling” and the SNR evolution would not be properly resolved. We conclude that it is unsafe to use a criterion  $\mathcal{R}_M \sim 1$  unless the material within the feedback region is reset to a uniform density (see below). More generally, to avoid vulnerability to overcooling, we use as small a feedback region as possible, so as to make  $\mathcal{R}_M$  as close as possible to 0.027. This stricter criterion corresponds to  $\Delta x/r_{\text{sf}} = 1/10$  for  $R_{\text{snr,min}} = 3\Delta x$ , the “consistent convergence condition” of KO15a. If a SN event occurs in a very rarefied medium, such that  $\mathcal{R}_M < 0.027$  for  $R_{\text{snr,min}}$ , we increase  $R_{\text{snr}}$  and recalculate  $\mathcal{R}_M$  until  $\mathcal{R}_M > 0.027$ , then assign ST type feedback as above. Increasing  $M_{\text{snr}}$  from extremely small values reduces the initial temperature from extremely high values, that would otherwise lead to extremely short time steps.

Finally, in the case that the surrounding medium has density so low that  $\mathcal{R}_M < 0.027$  even for  $R_{\text{SNR}} = R_{\text{snr,max}}$ , we assign pure kinetic energy within the remnant. We refer to this type of feedback as EJ, as it represents the effects of ejecta in the free expansion stage.

For ST and EJ feedback, the mass density, momentum density, and internal energy of the gas within a SN feedback region are initially set to constant values using the mean density, mass-weighted mean velocity, and mean internal energy, respectively, within  $R_{\text{snr}}$ . We then assign additional momentum with a radial velocity profile of  $v_r \propto r^2$  and uniform thermal energy within  $R_{\text{snr}}$ . Note that the ejecta mass is already added in prior to calculation of the mean density.

For MC feedback, we do not reset the gas properties in the feedback region prior to applying the momentum associated with the SN event. When we assign velocity fields, we add corresponding radial momentum to each gas parcel’s momentum in the star particle’s rest frame. In low-resolution

simulations (used for our convergence test), more than one SN event can be assigned at a given time and position. We then additively inject momentum and energy from multiple SNe.

To demonstrate the results of our SN feedback method, we run test simulations of radiative SNR evolution in a uniform medium with fixed spatial resolution of  $\Delta x = 4 \text{ pc}$ . Figure 6 plots (a) final radial momentum and (b) the maximum mass of hot gas ( $T > 10^5 \text{ K}$ ), both as a function of the number density of the ambient medium ( $n_{\text{amb}}$ ; bottom axis) and the enclosed mass of the feedback region ( $M_{\text{snr}}$ ; top axis). Results using our fiducial prescription as described above are shown in blue. For comparison, we also show the result of using purely thermal energy injection (green) and purely kinetic energy injection (red) within a radius of  $R_{\text{snr,min}} = 3\Delta x$ . For reference, symbols connected with dotted lines indicate the corresponding initial values of (a) radial momentum and (b) hot gas mass, as applied by the different feedback prescriptions. In Figure 6(b), the dotted blue and green lines coincide for  $\Delta x/r_{\text{sf}} < 1/3$ . The vertical dashed lines denote  $\Delta x/r_{\text{sf}} = 1/10$  and  $1/3$ , where  $r_{\text{sf}} = 22.6 \text{ pc} (n_{\text{amb}} / \text{cm}^{-3})^{-0.42}$  is the shell formation radius at the corresponding ambient density (KO15a). The vertical line at  $\Delta x/r_{\text{sf}} = 1/3$  corresponds to the transition from the ST (at lower density) to the MC (at higher density) feedback type in our prescription. Note that the transition to EJ type feedback would occur for  $n_{\text{amb}} < 9 \times 10^{-4} \text{ cm}^{-3} (R_{\text{snr,max}} / 128 \text{ pc})^{-2.38}$ , beyond the domain of this figure.

In both panels, if the Sedov–Taylor stage is fully resolved (according to the assessment of KO15a) with  $\Delta x/r_{\text{sf}} < 1/10$ , all feedback prescriptions give the same result for both final energy and maximum hot gas mass. As the Sedov–Taylor stage is marginally resolved with  $\Delta x/r_{\text{sf}} = 1/3$ , the different prescriptions lead to a factor of a few differences. In particular, Figure 6(a) indicates that the final momentum is significantly under- and over-estimated for unresolved cases ( $\Delta x/r_{\text{sf}} > 1/3$ ) when feedback is implemented via purely thermal and kinetic energy, respectively. Our fiducial method injects momentum to the medium within 25% (gray shaded region) of that found by KO15a for all values of the density. We note that the cooling curve and the treatment of the mean molecular weight are slightly different from those of KO15a, such that agreement in the overall trend is more important than absolute values. If  $\Delta x/r_{\text{sf}} < 1/3$ , the hot gas mass peaks at around the shell formation time and remains within  $\sim 25\%$  of KO15a. If  $\Delta x/r_{\text{sf}} > 1/3$ , as the initial SNR size  $R_{\text{snr}} = R_{\text{snr,min}} = 3\Delta x$  is larger than the shell formation radius, the hot gas mass peaks initially and then drops abruptly for all cases. For these unresolved cases, the hot gas mass is initially overestimated, but at later times is severely underestimated relative to resolved simulations (with smaller  $\Delta x$ ) at the same  $n_{\text{amb}}$ .

Careful inspection of the final momentum for the case where  $\Delta x/r_{\text{sf}} = 1/3$  and  $\mathcal{R}_M = 1$  (i.e.,  $M_{\text{snr}} = 1000 M_\odot$ , near the right vertical dashed line in Figure 6(a)), shows that both kinetic and thermal prescriptions lead to deviations from the correct solution. Thus, if one wanted to adopt a pure thermal feedback for resolved regions (i.e., low  $M_{\text{snr}}$ ) and MC feedback for unresolved regions, it would be necessary to choose  $M_{\text{snr}} \sim 400 M_\odot$  rather than  $M_{\text{snr}} = 1000 M_\odot$  as the transition point. In a clumpy medium, even the lower value of  $M_{\text{snr}}$  might be risky. We note that Gatto et al. (2017, see also Gatto et al. 2015) adopt for their resolved treatment (applied when  $\mathcal{R}_M < 1$ ) a pure-thermal prescription with a feedback region size chosen such that  $M_{\text{snr}} = 1000 M_\odot$ . Based on our analysis, that size

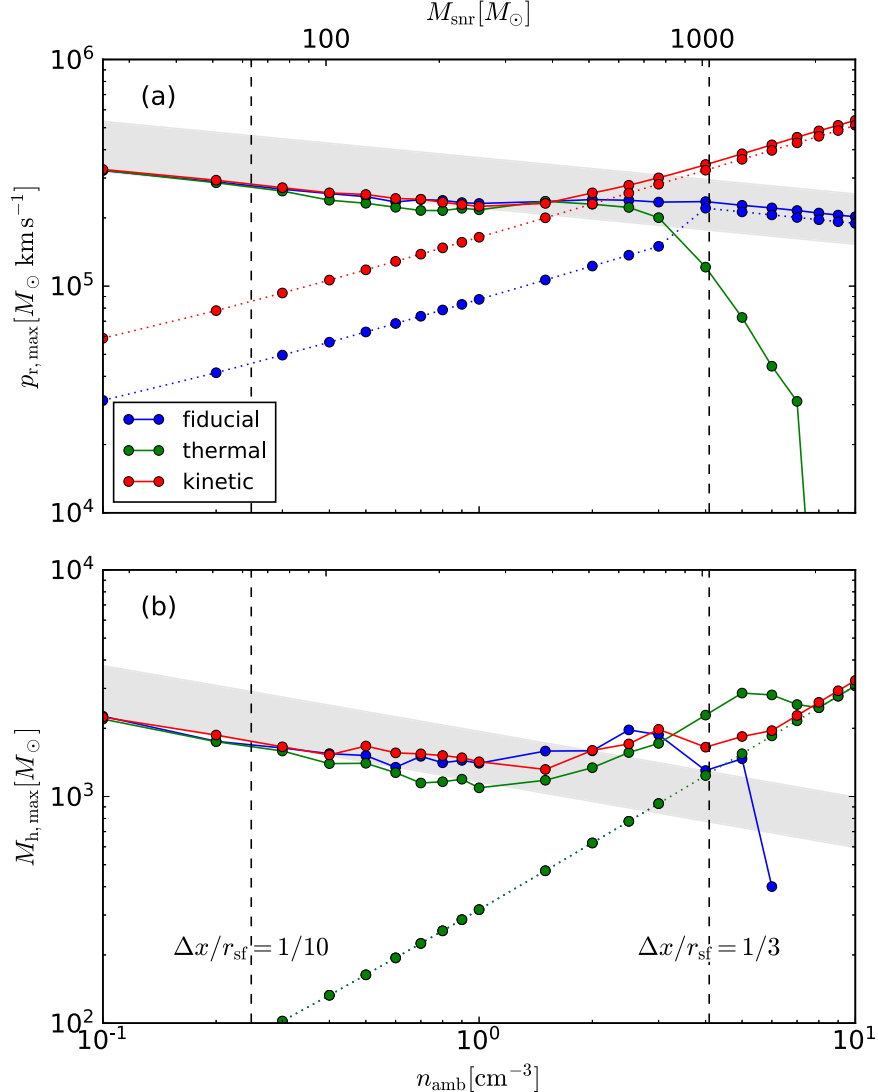


**Figure 6.** Tests of SN feedback prescriptions, based on simulations of radiative SNR evolution in a uniform medium with spatial resolution of  $\Delta x = 4$  pc: (a) the final radial momentum and (b) the maximum mass of hot gas ( $T > 10^5$  K), both as a function of the number density of the ambient medium ( $n_{\text{amb}}$ ). Blue symbols connected with solid lines show results based on our fiducial feedback prescription, as described in the text. Green and red symbols connected with solid lines show results of purely thermal and purely kinetic energy feedback methods, respectively. Symbols connected with dotted lines indicate the initial values of radial momentum and hot gas mass for different feedback methods. The dashed vertical lines demarcate loci of different resolution for the initial SNR of radius  $r_{\text{sf}} = 22.6 \text{ pc} (n_{\text{amb}} / \text{cm}^{-3})^{-0.42}$  (KO15a), with  $\Delta x / r_{\text{sf}} = 1/10$  (left) and  $\Delta x / r_{\text{sf}} = 1/3$  (right). The gray shaded regions in (a) and (b), respectively, enclose fitting results from KO15a within  $\pm 25\%$  for the final momentum  $p_{\text{final}} = 2.95 \times 10^5 (n_{\text{amb}} / \text{cm}^{-3})^{-0.16} M_{\odot} \text{ km s}^{-1}$  and the hot gas mass at shell formation  $M_{\text{sf}} = 1.55 \times 10^3 (n_{\text{amb}} / \text{cm}^{-3})^{-0.29} M_{\odot}$ .

would be marginal. Also, because Gatto et al. did not redistribute mass to make the density in the feedback region uniform in the thermal-feedback case, it would make their treatment even more vulnerable to overcooling, as described above. Overcooling may potentially explain why their SN-only model results in quite high SFRs, while our SN-only SFRs are much lower (and consistent with observations). Note that a feedback prescription that transitions from EJ type (red line in Figure 6) to MC type feedback at  $M_{\text{snr}} \sim 400 M_{\odot}$  can also inject the correct momentum (and produce hot gas if resolved). The SN feedback prescriptions described in Kimm & Cen (2014) and Hopkins et al. (2014) use an EJ-transitioning-to-MC approach.

#### 2.4. Gas Phases

We distinguish the gas in simulations by defining five components: cold ( $c$ )  $T < 184$  K; unstable ( $u$ )  $184 \text{ K} <$

$T < 5050$  K; warm ( $w$ )  $5050 \text{ K} < T < 2 \times 10^4$  K; ionized ( $i$ )  $2 \times 10^4 \text{ K} < T < 5 \times 10^5$  K; hot ( $h$ )  $T > 5 \times 10^5$  K. We use the Heaviside step function  $\Theta(C)$  to filter each component, where  $C = c, u, w, i, h$ . Sometimes we refer to  $C = c + u + w$  as warm-cold medium (wc) and to  $C = i + h$  as hot-ionized medium (hi). In the analysis below, we define summation of the quantity  $Q$  over each component as  $\sum_C Q \equiv \sum Q \Theta(C)$ .

### 3. Fiducial Solar Neighborhood Model

In this section, we begin by describing the evolution of a solar neighborhood model with standard resolution,  $\Delta x = 4$  pc. The simulation domain size is  $L_x = L_y = 1024$  pc and  $L_z = 4096$  pc. We limit the maximum SN feedback region radius to  $R_{\text{snr},\text{max}} = 128$  pc. For the external gravity (Equation (6)), we use the parameter set determined by Zhang

et al. (2013),  $\Sigma_* = 42 M_\odot \text{ pc}^{-2}$ ,  $z_* = 245 \text{ pc}$ ,  $\rho_{\text{dm}} = 0.0064 M_\odot \text{ pc}^{-3}$ , and  $R_0 = 8 \text{ kpc}$ . In the limit of  $|z| \ll z_*$ , the external gravity can be approximated by a linear profile  $g_{\text{ext}} \approx -4\pi G \rho_{\text{sd}} z$ . In our previous work (e.g., Kim et al. 2013; Kim & Ostriker 2015b, which had smaller vertical domain than is required to follow the hot ISM and wind launching), we used  $\rho_{\text{sd}} = 0.05 M_\odot \text{ pc}^{-3}$  for the volume density of stars and dark matter at the midplane in the solar neighborhood. The current parameter set gives a larger value of  $\rho_{\text{sd}} = \Sigma_*/(2z_*) + \rho_{\text{dm}} = 0.092 M_\odot \text{ pc}^{-3}$ . We adopt  $\Omega = 28 \text{ km s}^{-1} \text{kpc}^{-1}$ , which yields  $t_{\text{orb}} = 220 \text{ Myr}$ , and binary OB fraction  $f_{\text{bin}} = 2/3$ .

For the initial vertical gas-density profile, we use a double exponential

$$\rho(z) = \rho_1(z) + \rho_2(z) = \rho_{10} \exp(-\Phi_{0,\text{tot}}(z)/\sigma_1^2) + \rho_{20} \exp(-\Phi_{0,\text{tot}}(z)/\sigma_2^2), \quad (28)$$

where  $\Phi_{0,\text{tot}}(z) = \Phi_{\text{ext}}(z) + 2\pi G \Sigma |z|$  is the total gravitational potential using a thin-disk approximation for gaseous self-gravity. The adopted initial effective sound speeds of two phases are set to  $\sigma_1 = 7 \text{ km s}^{-1}$  and  $\sigma_2 = 10\sigma_1$ , respectively, representing warm and hot media. The midplane density of the warm medium is  $\rho_{10} = 2.85 m_H \text{ cm}^{-3}$ , while for the hot medium  $\rho_{20} = 10^{-5} \rho_{10}$ , such that it has negligible mass contribution. The total initial gas surface density is  $\Sigma = 13 M_\odot \text{ pc}^{-2}$ . The initial pressure profile is set to  $P = \rho_1 \sigma_1^2 + \rho_2 \sigma_2^2$ . The initial magnetic fields have only azimuthal ( $\hat{y}$ ) components with constant plasma beta,  $\beta \equiv 8\pi P/B^2 = 10$ , everywhere. This yields an initial midplane magnetic field strength of  $B = 2.6 \mu G$ . The initial heating rate is set to  $\Gamma_0$ .

Our initial conditions are not in thermal equilibrium, and the density near the midplane is higher than the maximum density of the WNM for given cooling and heating rates. As soon as the simulation begins, the gas immediately cools and loses vertical support from thermal pressure. Thermal instability develops rapidly and separates the gas near the midplane into the CNM and WNM. As a consequence, if the system is initiated without any turbulent support, the CNM falls to the midplane and forms a very thin and dense slab (e.g., Kim et al. 2010). This leads to very bursty star formation, making the overall evolution converge slowly.

In order to reduce the artificial initial burst of star formation (and subsequent “ringing”), for an initial period we drive turbulence that provides overall vertical support. At the same time, compressions seeded by these initial velocity perturbations enhance thermal instability and promote star formation. We use one-dimensional velocity power spectrum  $\mathcal{P}_k \propto k^{-2}$  for  $1 < kL_x/2\pi < 64$ , with driving rate  $\dot{E}_{\text{turb}} = 10^4 L_\odot$ . Turbulence is driven with this full strength for 50 Myr, and then slowly turned off from 50 Myr to 100 Myr. During the driving phase, we place a minimum on the heating rate of  $\Gamma_0$  for the first 50 Myr, and reduce this minimum slowly as the turbulent driving decreases. As stars form, turbulence and heating driven by SN and FUV feedback begin to exceed the imposed turbulent driving and minimum heating rate. All of our quantitative assessments are made after the artificial driving/heating phase has ended and a quasi-steady saturated state has been reached. We have confirmed that evolution and properties in the saturated state are insensitive to the exact form of initial turbulent driving and heating. The exact initial density and pressure profiles are also unimportant.

### 3.1. Overall Evolution and Star Formation Cycles

Figure 7(a) shows time evolution of the recent SFR surface density calculated using the total mass of young stars;

$$\Sigma_{\text{SFR}}(\Delta t = t_{\text{bin}}) \equiv \frac{\sum m_{\text{sp}}(t_{\text{m}} < t_{\text{bin}})}{L_x L_y t_{\text{bin}}} \quad (29)$$

We choose three different bins,  $t_{\text{bin}} = 10, 40$ , and  $100 \text{ Myr}$ , to indicate the way of SFR surface density would vary when traced by different diagnostics of young stars (e.g., the simple burst model adopted in Leroy et al. 2012 would have 95% of H $\alpha$  and FUV emitted within 4.7 Myr and 65 Myr, respectively). As the early driven turbulence effectively limits the bursty behavior in the initial star formation,  $\Sigma_{\text{SFR}}$  increases with only a factor of a few variation up to  $t \sim 100 \text{ Myr}$ . After this early “imposed driving” phase, star formation feedback self-consistently offsets cooling and drives turbulence. Time evolution after  $t = 100 \text{ Myr}$  reaches a quasi-steady state with self-regulation cycles involving large amplitude temporal fluctuations in  $\Sigma_{\text{SFR}}$ . In each cycle, gas falls to the midplane and is collected by self-gravity and large-scale turbulent flows into giant clouds, where collapse occurs in the highest density regions. The massive stars in the newly born clusters that form strongly increase the FUV radiation field and SN rate, which disperses the dense gas and enhances heating and turbulent driving throughout the ISM. Star formation shuts off as the gas disk puffs up and becomes warmer. With the corresponding reduction in star formation feedback, gas can settle back to the midplane and once again collect into large clouds where star formation occurs. The mean duty cycle is  $\sim 45 \text{ Myr}$  for the simulation shown, and there is an order of magnitude variation in  $\Sigma_{\text{SFR}}(\Delta t = 10 \text{ Myr})$ . For  $\Sigma_{\text{SFR}}(\Delta t = 40 \text{ Myr})$  there is less than a factor of two variation, and for  $\Sigma_{\text{SFR}}(\Delta t = 100 \text{ Myr})$  it is only 10–20%. It should be kept in mind, however, that the amplitude of variations depends on the horizontal box size, because it determines the number of independent star-forming patches. Larger boxes that contain a larger number of independent patches would have reduced variation in  $\Sigma_{\text{SFR}}(\Delta t = 10 \text{ Myr})$ .

Figure 7(b) plots time evolution of the surface density of FUV luminosity  $\Sigma_{\text{FUV}} = L_{\text{FUV}}/L_x L_y$  normalized by  $\Sigma_{\text{FUV},0}$  to show the time evolution of the heating rate. As seen in Figure 5, most FUV comes from very massive stars in star clusters younger than  $\sim 10 \text{ Myr}$ . Therefore, the temporal variation of the heating rate is very similar to  $\Sigma_{\text{SFR}}(\Delta t = 10 \text{ Myr})$ . Similar to  $\Sigma_{\text{SFR}}(\Delta t = 10 \text{ Myr})$ , there is an order of magnitude temporal fluctuation in the amplitude of  $\Sigma_{\text{FUV}}$ .

Figure 7(a) shows a secular decrease of  $\Sigma_{\text{SFR}}$  over time, which is clearest in 40 Myr and 100 Myr averages. This reduction is mainly because the total gas mass decreases, as seen in Figure 7(c); there we show time evolution of gas, star, and outflow mass fractions compared to the initial gas mass. In this simulation, we convert gas into sink/star particles, but we do not replenish it. Also, a significant amount of the gas flows out through vertical boundaries in the form of hot winds and warm fountains driven by the clustered SN feedback (and SNe from runaways at high- $|z|$ ).<sup>3</sup> Considering the secular evolution of the simulation, we limit our analysis of statistical properties

<sup>3</sup> The driving and properties of winds and fountains are an important aspect of our simulations (as well as real galaxies) and will be carefully analyzed in a forthcoming companion paper.

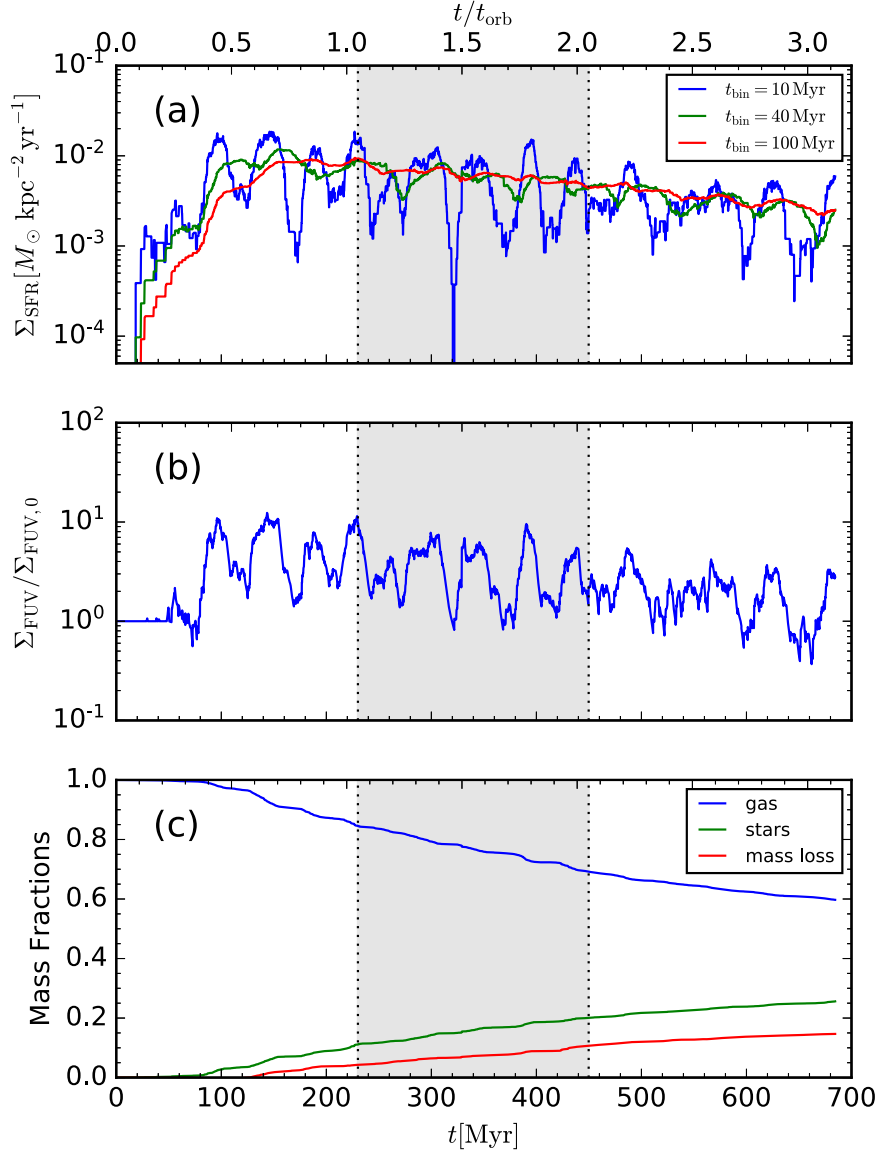


**Figure 7.** Time evolution of (a) surface density of SFR,  $\Sigma_{\text{SFR}}$ , for star clusters younger than 10 (blue), 40 (green), and 100 (red) Myr; (b) surface density of FUV luminosity,  $\Sigma_{\text{FUV}}$ , in units of  $\Sigma_{\text{FUV},0} = 6.9L_{\odot}/\text{pc}^2$ ; and (c) mass fractions of gas (blue), new stars (green), and gas mass loss through the vertical boundaries (red) compared to initial total gas mass. The shaded region between vertical dotted lines denotes the time range for  $11 > \Sigma/(M_{\odot} \text{ pc}^{-2}) > 9$  over which statistical properties are calculated.

to the time range between  $t_1 = 1.05t_{\text{orb}} = 231$  Myr and  $t_9 = 2.05t_{\text{orb}} = 450$  Myr (shaded region in Figure 7), corresponding to the times when the gas surface density is  $11 M_{\odot} \text{ pc}^{-2}$  and  $9 M_{\odot} \text{ pc}^{-2}$ , respectively. This is reduced from an initial gas surface density of  $13 M_{\odot} \text{ pc}^{-2}$ .

Figure 8 displays a series of five-panel snapshots showing surface density projections and number density and temperature slices at an interval of  $0.05t_{\text{orb}} \sim 11$  Myr, starting at  $t = 1.8t_{\text{orb}} = 395$  Myr. Sink and star particles are also shown (see caption for details). For one selected time  $t = 1.95t_{\text{orb}} = 428$  Myr when a strong outflow driven by SNe is prominent, Figure 9 shows the distribution of sink/star particles, number density, temperature, vertical velocity, and magnetic field strength.

The series of snapshots in Figure 8 clearly shows the characteristic evolutionary cycle of self-regulated star formation. In the first snapshot (at  $t = 1.8t_{\text{orb}}$ ), a collection

of star clusters has formed in a dense cloud complex slightly below the center of the XY plane. These young clusters heat up the gas and evaporate most of the CNM. As a result, the WNM predominates in the midplane (see temperature slice), although the hot gas still fills  $\sim 20\%$  of the volume near the midplane. These sink/star particles produce a large number of SN explosions (from  $t = 1.8t_{\text{orb}}$  to  $t = 1.9t_{\text{orb}}$ ), and consequently a superbubble forms, clearly evident in the low-density and high-temperature regions of the XY panels of the  $t = 1.9t_{\text{orb}}$  snapshots. At this epoch, the sink/star particles from this burst have aged (see color scale) and emit less FUV radiation. Plenty of the CNM can now form within the WNM, as is evident in the XY temperature panel at  $t = 1.9t_{\text{orb}}$ . As the hot bubble occupies more than the half of the volume near the midplane, the CNM/WNM is pushed aside and aggregated within a smaller volume outside of the bubble. Within this favorable environment, a massive, dense

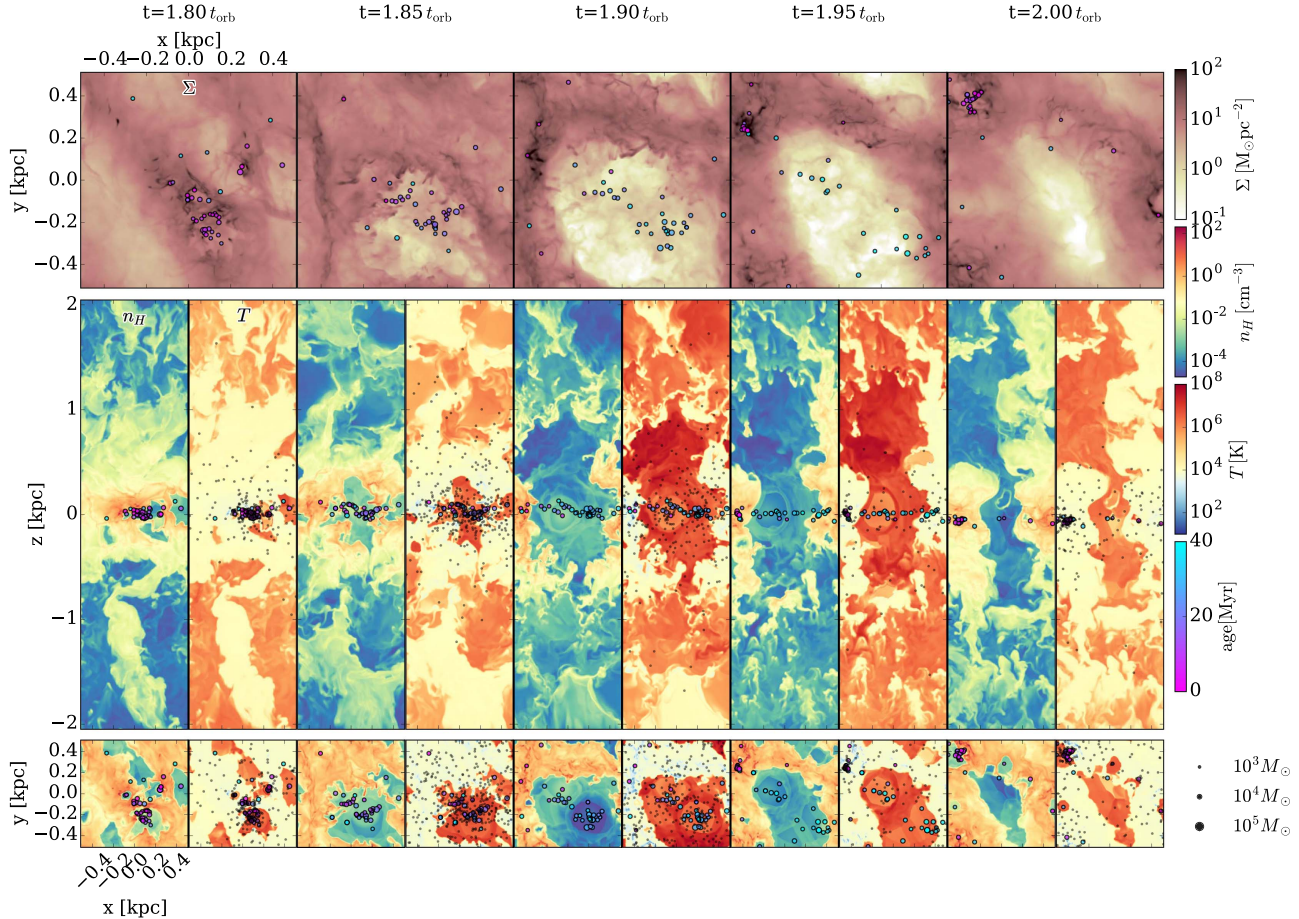


**Figure 8.** Time evolution of the ISM and young star population in the solar neighborhood model, shown at intervals of  $\Delta t = 0.05 t_{\text{orb}} \approx 11$  Myr, from  $t = 1.8 t_{\text{orb}} = 395$  Myr to  $t = 2 t_{\text{orb}} = 439$  Myr. Top row: gas surface density  $\Sigma$  projected onto the XY ( $\hat{x}-\hat{y}$ ) plane. Middle row: paired vertical slices (through  $y = 0$ ) of number density  $n_{\text{H}}$  (left) and gas temperature  $T$  (right). Bottom row: paired midplane slices (through  $z = 0$ ) of  $n_{\text{H}}$  (left) and  $T$  (right). In all panels, colored circles denote locations of all sink and star particles younger than 40 Myr (see the colorbar) projected onto each plane. The symbol size of sink/star particles denotes their mass (see legend). Runaway OB stars are shown as black dots only in the temperature panels for visual clarity.

cloud assembles (upper left of XY panel) and promotes a second round of star formation (see snapshots at  $t = 1.95$  and  $2t_{\text{orb}}$ ). At  $t = 2t_{\text{orb}}$  (last set of snapshots), the first hot bubble has mostly merged with surrounding gas, as its interior has cooled off and turbulence redistributes material into the former bubble volume. Meanwhile, the result of new star formation is evident in the upper-left corner of the midplane. The feedback from this collection of sink/star particles will produce another superbubble. This cycle of massive cloud assembly leading to a burst of star formation, followed by a burst of feedback leading to star formation quenching, continues throughout the run.

Breakout of superbubbles from the warm-cold midplane layer drives hot gas to high- $|z|$ ; e.g., the XZ slices at  $t = 1.9$  and  $1.95 t_{\text{orb}}$  in Figure 8 show this clearly. As shown in Figure 9, the hot gas has high outward vertical velocity, i.e., large  $|v_z|$  at large  $|z|$ , with  $\text{sign}(v_z) = \text{sign}(z)$ . We anticipate that this rapidly expanding hot outflow would escape to the CGM and/or IGM as a galactic wind. From Figures 8 and 9, substantial WNM is also pushed to high- $|z|$  by superbubble expansion. However, outward vertical velocities of this warm material are insufficient to escape the gravitational potential of the galaxy ( $|v_z| > 200$  km s $^{-1}$  would be required). The majority of the WNM falls back toward the midplane (when feedback is at a low state), creating the “return flow” of a galactic fountain. Detailed analysis of the multiphase

high- $|z|$  wind and fountain flows is deferred to the companion paper.

### 3.2. Multiphase Structures and Turbulence Properties of the ISM

The ISM material in our simulation populates a wide range of temperatures, with three distinct phases. Figure 10 plots probability density distributions (PDFs) of gas temperature weighted by mass (blue) and volume (green). Thermal instability and rapid cooling tend to reduce the amount of gas in the unstable (UNM) and ionized components. However, strong turbulence, large temporal fluctuations of the heating rate, and expanding superbubbles in our simulation continuously repopulate these regimes. In addition, because our numerical resolution is not high enough to spatially resolve the transition layer between the WNM and CNM, the CNM (UNM) mass fraction may be numerically reduced (enhanced).<sup>4</sup> Therefore, for studying numerical convergence,

<sup>4</sup> With our adopted numerical resolution, we cannot fully resolve the Field length for realistic thermal conductivity. However, Kim et al. (2008) showed that numerical diffusion caused by translational motion produces an effective “numerical conductivity” that is much larger than the physical thermal conductivity. The phase transition layer is thicker and the UNM mass fraction increases as the numerical resolution gets poorer (increasing “numerical conductivity”). As a consequence, the CNM mass fraction decreases at low resolution, while the WNM mass fraction remains the same.

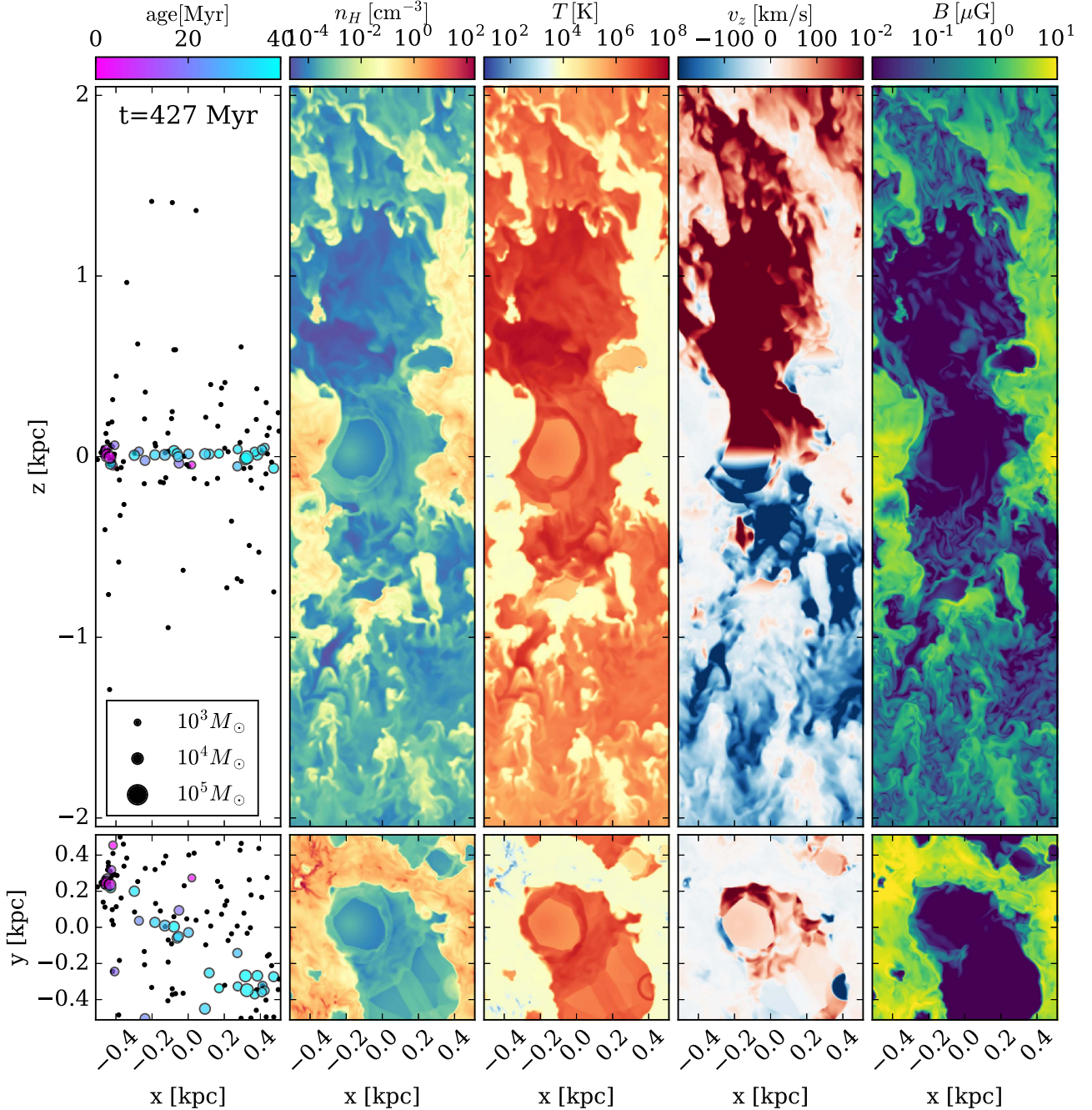


**Figure 9.** Snapshots of (a) sink/star particles, (b) number density, (c) temperature, (d) vertical velocity, and (e) magnetic field strength at  $t = 1.95t_{\text{orb}} = 428$  Myr. At this time, a strong outflow is driven by SN-heated gas. In columns (b)-(e), we present XZ (through  $y = 0$ ; top) and XY (through  $z = 0$ ; bottom) slices of ISM properties. In column (a) positions of sink/star particles with age younger than 40 Myr (colored circles) and runaway stars (black dots) are projected onto XZ (top) and XY (bottom) planes.

we will consider the mass fraction of the CNM plus UNM, rather than their individual fractions. We obtain mean mass fractions between  $t_{11}$  and  $t_9$  of  $f_{c+u} = 24\%$  and  $f_w = 75\%$ .

Figure 11 displays gas PDFs at  $t = 1.95t_{\text{orb}} = 428$  Myr (top row) and averaged over time ranges between  $t_{11} = 1.05t_{\text{orb}} = 231$  Myr and  $t_9 = 2.05t_{\text{orb}} = 231$  Myr (bottom row) weighted by mass (left column) and volume (right column) in the  $n_{\text{H}} - P/k_B$  phase plane. We draw the locus  $T = 1.2 \times 10^6$  K as a dashed line representing a typical hot gas temperature defined by the peak of the volume PDF (Figure 10) for the hot-ionized medium. The dotted line in (a) and (b) shows the instantaneous thermal equilibrium curve for

$\Gamma = 3.8\Gamma_0$ . Two dotted lines in (c) and (d) show the thermal equilibrium curves for  $\Gamma = \Gamma_0$  and  $\Gamma = 10\Gamma_0$ , which approximately brackets the variation in heating rate from the varying  $\Sigma_{\text{FUV}}$  shown in Figure 7(b). The mass PDF shows that the CNM, UNM, and WNM components are the most populated, while the volume PDF is dominated by the WNM, ionized, and hot components.

The warm-cold medium ( $T < 2 \times 10^4$  K) tends to evolve to a two-phase state with a short cooling time, and the majority of the warm-cold medium indeed follows the instantaneous thermal equilibrium curve and is within the envelope of the two thermal equilibrium curves in Figure 11. However, due to strong turbulence and the large time variation in the heating rate, the

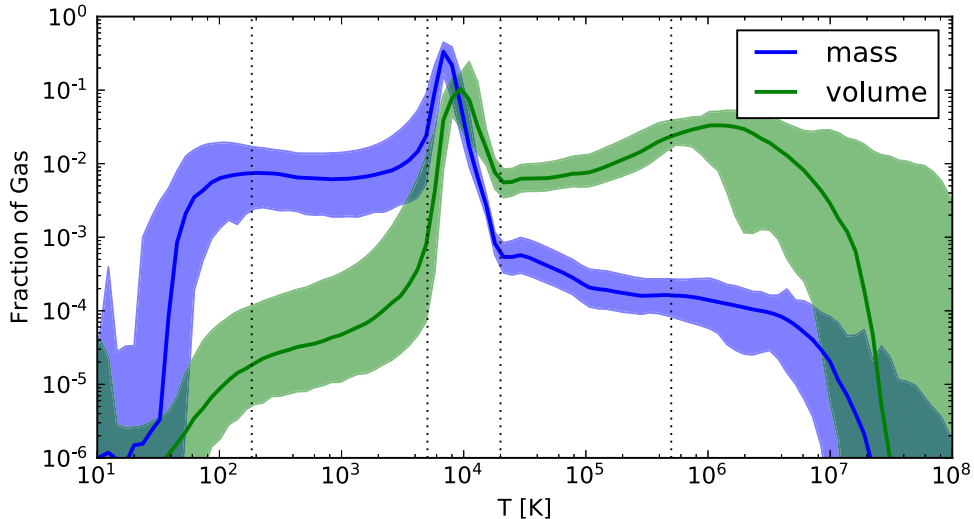


**Figure 10.** Temperature PDFs weighted by mass (blue) and volume (green). The solid lines denote the median value of each bin over the time span of  $t_{11}$ – $t_9$ , and the shaded area envelopes the minimum and maximum values over this time span. The vertical dotted lines indicate  $T = 184$  K,  $5050$  K,  $2 \times 10^4$  K, and  $5 \times 10^5$  K separating the gas into the five components we define (from left to right: CNM, UNM, WNM, ionized, and hot).

distinction between CNM and UNM is not as clear as expected from the classical theory (Field 1965; Field et al. 1969).

In the volume PDF, the WNM is strongly concentrated around thermal equilibrium, while the hot-ionized medium shows a broader distribution. At early stages of expansion for individual SN remnants or superbubbles, when the temperature of shock heated gas is high enough ( $T > 10^6$  K), adiabatically expanding hot interiors of bubbles form a sequence in the phase plane with a slope of  $5/3$ . As shown in Figure 10, the typical hot-ionized medium temperature ranges between  $10^6$  K and  $10^7$  K (Kim et al. 2017). As the shock expansion speed drops, the temperature of post-shock gas is lower, and due to the strong cooling peak at  $T \sim 10^5$  K (see Figure 1) this material quickly cools down to join the WNM. The centers of superbubbles remain hot until turbulence causes them to merge with the surrounding ISM. Thus, the volume PDF shows distinct hot and warm phases occupying the majority of the simulation volume. Continuous SN explosions and mixing maintain a non-negligible fraction of gas at intermediate temperature, between  $10^4$ – $10^6$  K.

Figures 12(a) and (b) plot time evolution averaged over the warm-cold medium ( $T < 2 \times 10^4$  K) of various mass-weighted velocities defined by

$$\begin{aligned} \sigma_i &\equiv \left( \frac{\sum_{wc} \rho \delta v_i^2 \Delta V}{\sum_{wc} \rho \Delta V} \right)^{1/2}, \quad c_s \equiv \left( \frac{\sum_{wc} P \Delta V}{\sum_{wc} \rho \Delta V} \right)^{1/2}, \\ \delta v_A &\equiv \left( \frac{\sum_{wc} \delta \mathbf{B} \cdot \delta \mathbf{B} \Delta V}{4\pi \sum_{wc} \rho \Delta V} \right)^{1/2}, \quad \bar{v}_A \equiv \left( \frac{\sum_{wc} \bar{\mathbf{B}} \cdot \bar{\mathbf{B}} \Delta V}{4\pi \sum_{wc} \rho \Delta V} \right)^{1/2}. \end{aligned} \quad (30)$$

Here,  $\sigma_i$  is the turbulent velocity dispersion in each direction,  $c_s$  is the sound speed,  $\delta v_A$  is the turbulent Alfvén speed, and  $\bar{v}_A$  is the mean Alfvén speed. The perturbed velocity (removing the background shear flow) is defined by  $\delta \mathbf{v} \equiv \mathbf{v} + q\Omega x \hat{\mathbf{y}}$ , the mean magnetic field  $\bar{\mathbf{B}}$  is calculated based on a horizontal average at each  $z$ , and the turbulent magnetic field is defined by  $\delta \mathbf{B} \equiv \mathbf{B} - \bar{\mathbf{B}}$ .

Turbulent velocity dispersions of the warm-cold medium are about  $11$  km s $^{-1}$  ( $\sigma_z \sim 5$  km s $^{-1}$  for the CNM and  $12$  km s $^{-1}$  for the WNM), a factor of 1.5 to 2 higher than those in our previous simulations (e.g., Kim et al. 2013; Kim & Ostriker 2015b), where we found  $\sigma \sim 5$ – $7$  km s $^{-1}$ . A number of effects could contribute to this increase in  $\sigma$ , including the correlation of supernovae in superbubbles and the cooling of hot gas that has expanded to large  $|z|$ . Note that the turbulent velocity dispersions fluctuate with a similar period to, but much lower amplitude than,  $\Sigma_{SFR}$ . Turbulent magnetic fields are generated very quickly by a turbulent dynamo (e.g., Kim & Ostriker 2015b), so that the turbulent Alfvén velocity is expected to quickly saturate, and indeed this rapid growth and saturation is seen. The turbulent magnetic field strength depends on both the turbulent kinetic energy and mean magnetic energy. As the mean field keeps growing for  $t < 400$  Myr, the saturation level of the turbulent magnetic energy also gradually increases in time. For  $t > 400$  Myr, the turbulent magnetic energy stays constant as the mean magnetic field strength reaches a certain level.<sup>5</sup> At this stage, the ratio between turbulent kinetic and magnetic energies is about 7:3, as in Kim & Ostriker (2015b). Growth of the mean magnetic field is slow, with the timescale similar to the orbit time, so that mean Alfvén velocity increases throughout the simulation.

In Figure 12(c), we show the scale heights of the CNM+UNM and WNM ( $C = c + u$ , and  $w$ , respectively) defined by

$$H_C \equiv \left( \frac{\sum_C \rho z^2 \Delta V}{\sum_C \rho \Delta V} \right)^{1/2}. \quad (31)$$

<sup>5</sup> Federrath et al. (2011) and Schober et al. (2012) have shown that the saturation level of the turbulent magnetic energy is much lower than the turbulent kinetic energy (less than a percent) for a dynamo driven by compressible turbulence, when the initial mean fields were almost negligible. Here, we instead find that turbulent magnetic energy saturates at a level similar to the turbulent kinetic energy. This may be due partially to our larger initial mean magnetic fields, and also in part to the presence of background sheared rotation. Understanding galactic dynamo behavior for realistic ISM turbulence combined with realistic shear, rotation, and vertical stratification is a very interesting question. However, this will require carefully controlled numerical studies and analyses, which we do not attempt here.

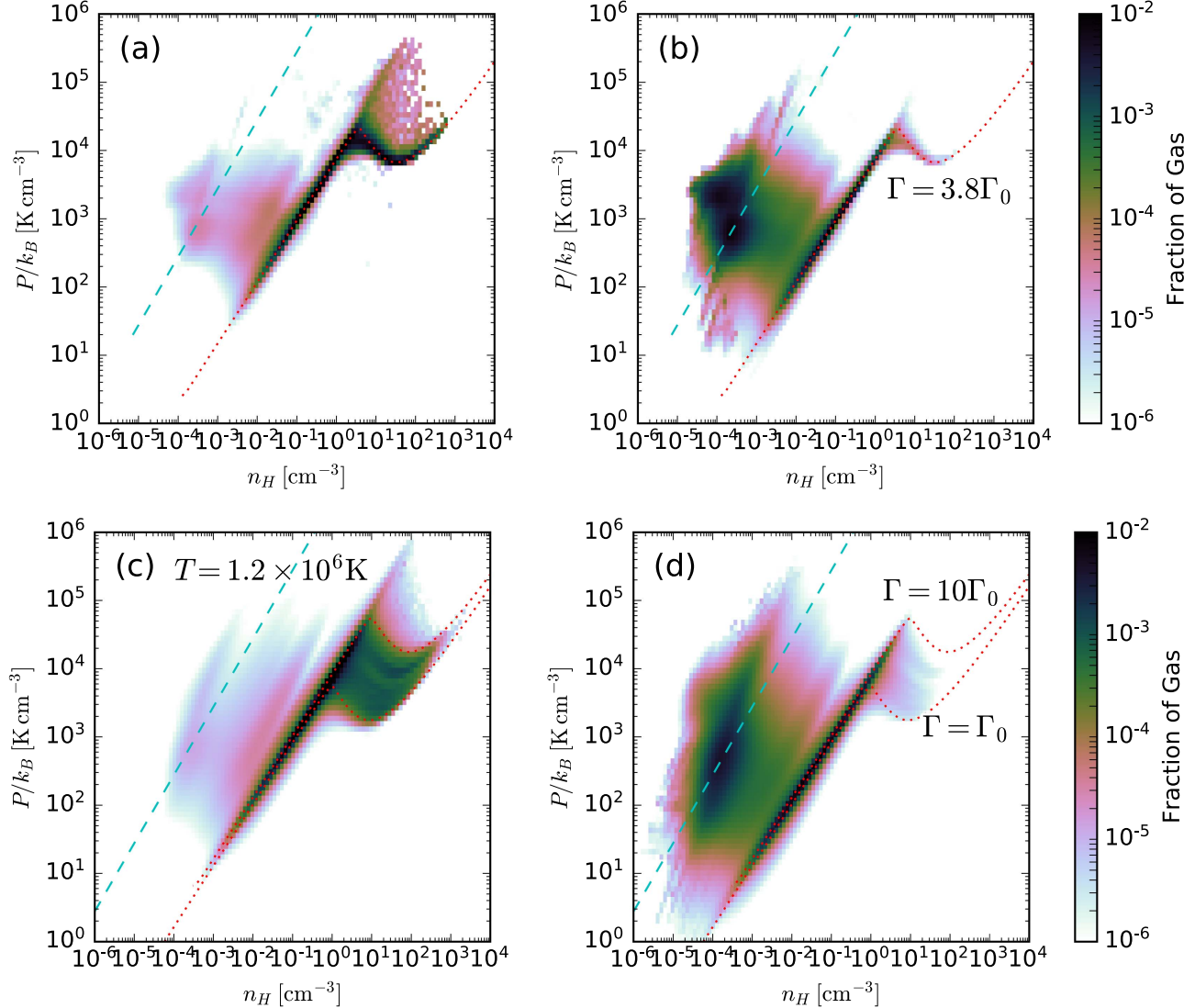


**Figure 11.** Instantaneous ( $t = 1.95t_{\text{orb}} = 427$  Myr; (a) and (b)) and time-averaged ( $t_{11-t_9}$  or  $1.05t_{\text{orb}}-2.05t_{\text{orb}}$ ; (c) and (d)) gas distribution in the number density ( $n_{\text{H}}$ ) and pressure ( $P/k_B$ ) phase plane. Color represents the mass (left column) and volume (right column) fractions in logarithmic bins. Dotted red lines denote the thermal equilibrium curves for instantaneous heating rate  $3.8\Gamma_0$  in (a) and (b) and representative heating rates  $\Gamma_0$  (lower) and  $10\Gamma_0$  (upper) in (c) and (d). The dashed cyan line denotes the typical temperature of the hot-ionized medium,  $T = 1.2 \times 10^6$  K.

Note that the vertical box size is not large enough to define a meaningful scale height for the ionized and hot components, so we omit these in this figure. The mean values of the scale heights averaged over  $t_{11-t_9}$  are  $H_{c+u} = 76$  pc and  $H_w = 363$  pc, giving a scale height of the warm-cold medium of  $H_{wc} = 317$  pc.

#### 4. Numerical Convergence

In this section, we compare statistical properties of the same solar neighborhood model run at different numerical grid resolutions, varying from  $\Delta x = 2$  pc to  $64$  pc. Hereafter, each model is referred as MHD- $\Delta x$ . Because all simulations secularly evolve due to the decline in gas mass, we obtain statistical properties over the range of times ( $t_{11}, t_0$ ) in each simulation when the gas is in the same gas surface density range of  $11 > \Sigma / M_{\odot} \text{ pc}^{-2} > 9$ , for the purpose of fair intercomparison. Before diving into the detailed quantitative comparison, in Figure 13 we display  $\Sigma$ ,  $n_{\text{H}}$ , and  $T$  snapshots at the respective times when  $\Sigma = 10 M_{\odot} \text{ pc}^{-2}$  (after saturation)

for all models. As expected, overdense structures and small-scale thermal variations are more smeared out as the resolution gets poorer. A discernible qualitative change only emerges with Model MHD-64pc, where we observe thermal runaway with highly correlated SNe that is not seen in higher-resolution models. However, as we shall show, Model MHD-32pc also diverges from higher-resolution simulations in many aspects, including both SFRs and ISM properties.<sup>6</sup> In models with higher resolution ( $\Delta x \leq 8$  pc), the WNM is ubiquitous at all  $z$ , and the hot-ionized medium fills substantial volume even near the midplane.

<sup>6</sup> It is important to note that, with insufficient resolution, the ISM properties fail to converge, in unpredictable ways. When we implemented SN feedback without allowing for overlap of SNRs at the same position and time, the result diverged in the opposite sense from what we describe here: Models MHD-32pc and MHD-64pc had no hot gas within the gas scale height. SN overlapping occurs frequently in low-resolution simulations, resulting in unrealistically highly correlated SNe and unphysical consequences for the ISM state.

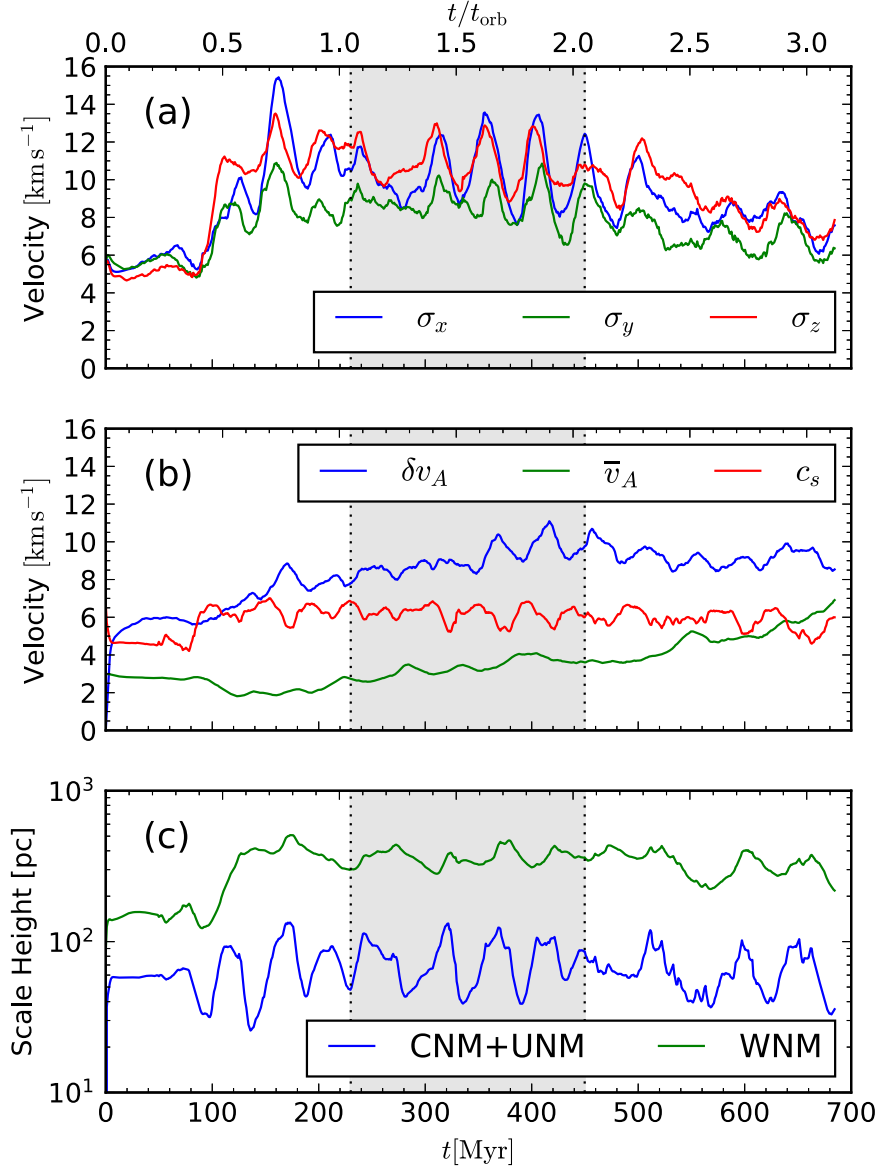


**Figure 12.** Time evolution of (a) turbulent velocity dispersions, (b) turbulent and mean Alfvén velocities and sound speed, and (c) scale heights. All quantities are averaged over the warm-cold medium. See text for definitions.

In the forthcoming subsections, we present SFRs and properties of the ISM measured during  $(t_{11}, t_9)$  using box-and-whisker plots to display key statistics as simply as possible. In these plots, the rectangular box extends from the 25th to 75th percentile of temporal fluctuations, and the median and mean are shown as a horizontal bar within the box and a square symbol, respectively. The whiskers extend to 5th and 95th percentiles with caps, and outliers are shown as circles.

#### 4.1. Star Formation Rates

In Figure 14, we first compare  $\Sigma_{\text{SFR}}$  using box-and-whisker plots for time in the interval  $(t_{11}, t_9)$ . Between the 25th and 75th percentile (box) with respect to the median value (horizontal bar in the box), all results except Models MHD-32pc and MHD-64pc are in good agreement. While  $\Sigma_{\text{SFR}}$  in Model MHD-32pc overlaps with the converged results, Model MHD-64pc has  $\Sigma_{\text{SFR}}$  several times larger than in the other models. As resolution gets poorer, the mass of star clusters gets larger, increasing stochasticity of the FUV luminosity. This leads to

large temporal fluctuations in  $\Sigma_{\text{SFR}}(t_{\text{bin}} = 10 \text{ Myr})$ , extending the 5th and 25th percentiles to zero for  $\Delta x \geq 16 \text{ pc}$ .

#### 4.2. Supernova Treatment

As described in Section 2.3.3, we have three different SN feedback treatments; the treatment that is applied for any given SN event depends on the parameter  $\mathcal{R}_M$  that represents the ratio of the mass that can be resolved in the feedback region around the SN compared to the expected SN remnant mass when it becomes radiative. At low numerical resolution, we expect that the Sedov–Taylor stage and shell formation in most SN explosions cannot be resolved (see KO15a), so they would be realized in the simulation with momentum feedback (type MC). At higher resolution, we instead expect the non-radiative early stage of evolution to be resolved in most cases, so that the ST type may be applied. In rare cases when the density is very low (mainly for SN events in superbubbles and at high- $|z|$  from runaways), the EJ type would be applied.

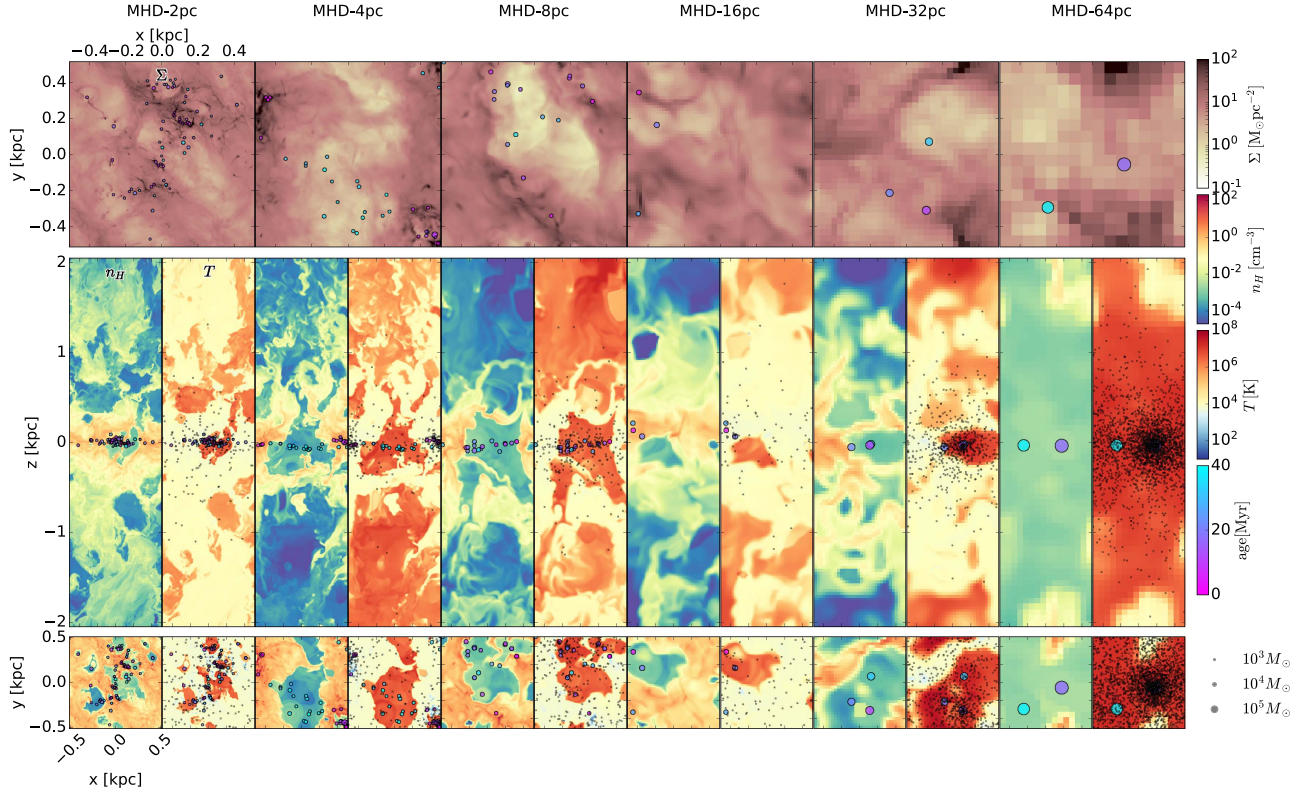


**Figure 13.** Comparison of structure at varying simulation resolution, for the same model parameters, when the gas surface density is  $\Sigma = 10 M_{\odot} \text{ pc}^{-2}$ , after a quasi-steady state has been reached. Each row shows the same properties as in Figure 8. Numerical resolution is poorer by a factor of two in each set from left to right, as labeled with  $\Delta x = 2 \text{ pc}, 4 \text{ pc}, 8 \text{ pc}, 16 \text{ pc}, 32 \text{ pc}$ , and  $64 \text{ pc}$ .

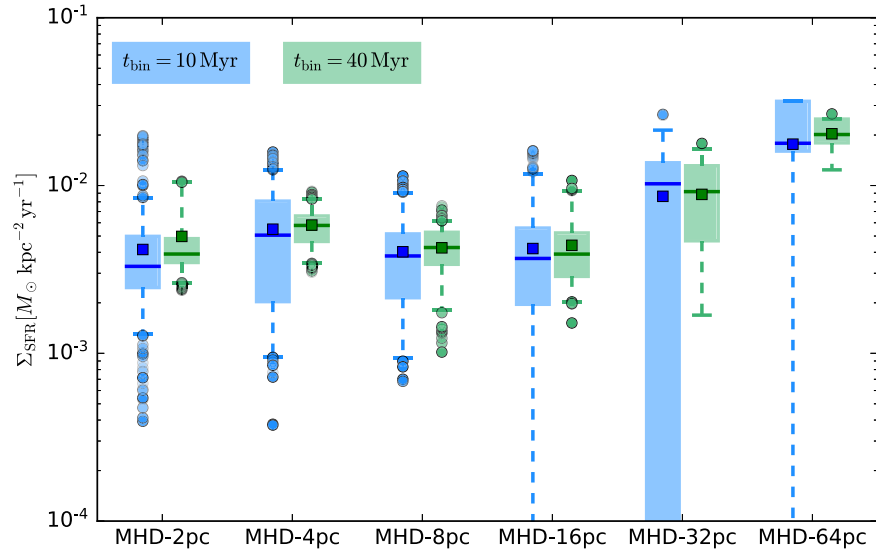


**Figure 14.** Dependence of SFR on numerical resolution. Models with resolution  $\Delta x \leqslant 16 \text{ pc}$  are converged. Box-and-whisker plots of  $\Sigma_{\text{SFR}}$  statistics for simulations with varying resolution. Boxes enclose the 25th to 75th percentiles with medians and means shown as horizontal bars and squares, respectively. Whiskers extend to the 5th and 95th percentiles (capped), with outliers shown as circles. For each model, we show side-by-side box-and-whisker plots for  $\Sigma_{\text{SFR}}$  computed with 10 Myr and 40 Myr time bins.

In Figure 15, panels (a) and (c) plot, for cluster and runaway SNe respectively, the cumulative fraction of SN events that occur with surrounding number density smaller than  $n_0$ . Panels (b) and (d) plot the fractions of SNe that are realized with each type of feedback, separately considering SNe from cluster and runaway star particles. Models up to  $\Delta x = 8 \text{ pc}$  have most of their SNe realized with the ST prescription (panels (b) and (d)),

meaning that the resolution is sufficient to follow evolution prior to the radiative stage. The fraction of pure momentum feedback (MC-type) increases as resolution gets poorer. In lower resolution models, SNe from cluster particles are more correlated and more effective at forming superbubbles (see Figure 13). Thus,  $n_0$  near SN sites is systematically lower for SNe in clusters when resolution is poor (panel (a) of Figure 15).

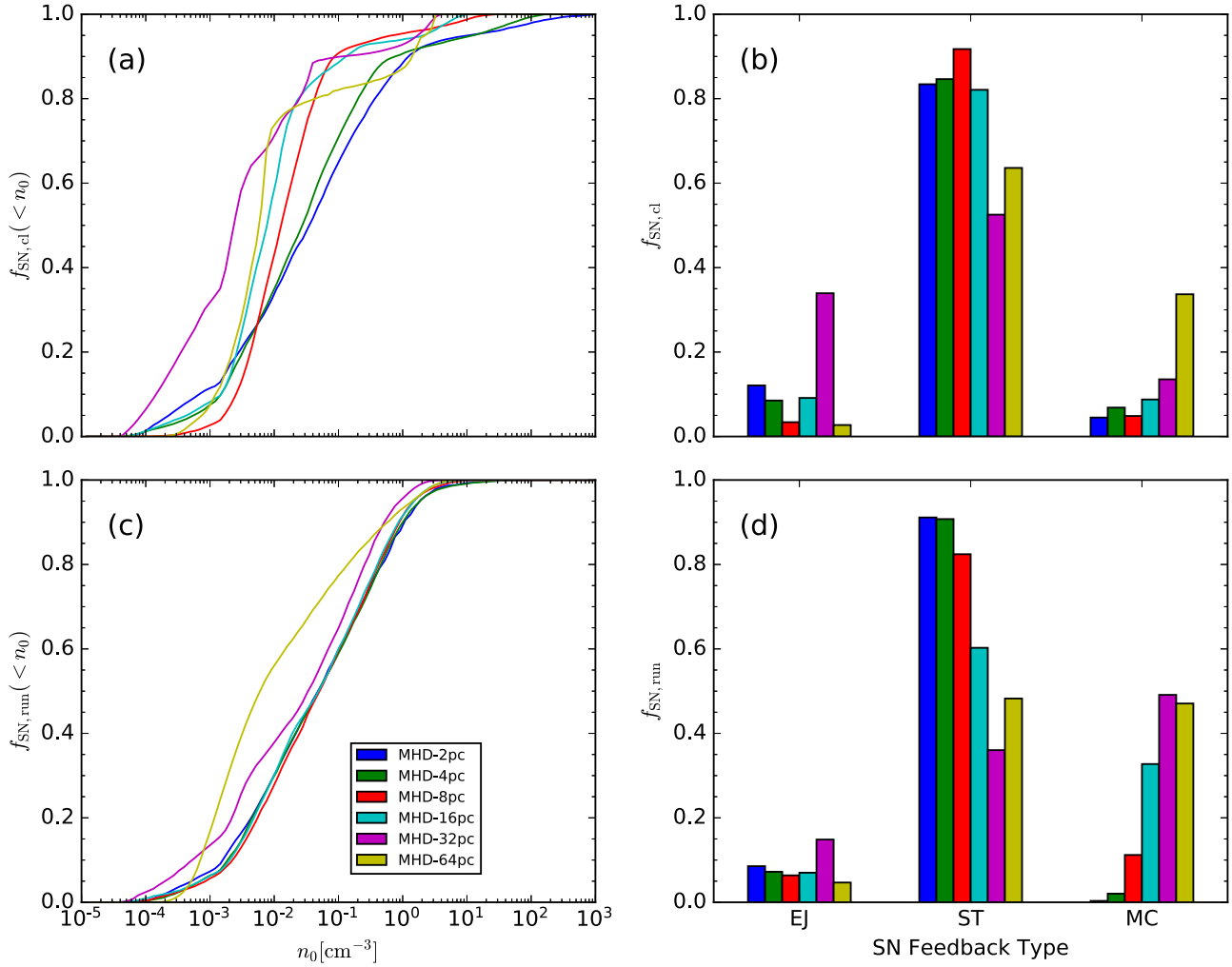


**Figure 15.** SN environment and feedback type distribution at varying resolution. (a) and (c): cumulative fraction of SN events that occur in regions where the surrounding density is smaller than  $n_0$ , for SNe in clusters and runaways, respectively. (b) and (d): fraction of SN feedback type for SNe in clusters and runaways, respectively. From Section 2.3.3, the type of feedback assigned depends on the ratio  $\mathcal{R}_M$  between the enclosed mass within the feedback region and expected remnant mass when it becomes radiative. The types correspond to different stages of evolution for the initial resolved remnant, and different methods of injecting energy and/or momentum. From earliest to latest evolutionary stage, these are: initial ejecta (EJ,  $\mathcal{R}_M < 0.027$ ), Sedov–Taylor (ST,  $0.027 < \mathcal{R}_M < 1$ ), and momentum-conserving (MC,  $1 < \mathcal{R}_M$ ). Note that the ratio of runaway SN events to cluster SN events is about 1/3 ( $f_{\text{bin}} = 2/3$ ).

However,  $n_0$  near sites of runaway SNe is rather insensitive to the resolution (panel (c)).

Not all SN events are realized with the ST or EJ prescriptions, even for the highest-resolution simulation. However, if there is a cluster in a very high-density region, one or two early SNe realized by momentum injection (MC) open a cavity such that subsequent SN events from the same cluster can be realized with the ST treatment. Implementation of early feedback such as stellar winds, radiation pressure, and photoionization could also help to open cavities around clusters and to achieve better convergence even for individual SN events at lower resolutions (e.g., runaway SNe in Model MHD-16pc).<sup>7</sup>

<sup>7</sup> Based on simulations including stellar winds and/or ionizing radiation (e.g., Gatto et al. 2017; Peters et al. 2017), some have argued that these feedback processes, rather than just SNe, are necessary to obtain accurate SFRs. However, spatial and temporal correlation of SN clustering are at least as important to the outcome as early feedback, so it is necessary to control for these effects (and confirm that they match observations) before reaching any conclusions. Our high-resolution simulations, which have only SN feedback, achieve a realistic SFR.

### 4.3. Turbulence and Phase Balance

In this subsection, we investigate the convergence of ISM properties, based on statistics for time in the range  $(t_{11}, t_9)$ . Figure 16 plots (a) vertical velocity dispersions, (b) turbulent Alfvén velocities, and (c) scale heights of the warm-cold medium using box-and-whisker plots. Models with  $\Delta x \leq 16$  pc are converged in these quantities, although the temporal fluctuations are much larger in Model MHD-16pc than in higher-resolution simulations. However, Models MHD-32pc and MHD-64pc show substantially larger velocity dispersions (panel (a)), and hence scale heights (panel (c)), in comparison to the resolved results. The spatial and temporal correlations of SNe are exaggerated in these models, with the result that overlapping multiple SNe drive large vertical (ordered) motions. While velocity dispersions and scale heights are large in low-resolution models, this is not due to higher-amplitude small-scale turbulence, but only to very large-scale correlated superbubble expansion. In fact, small-scale turbulence is *weaker* than in the high-resolution models, as can be seen in the in weaker turbulent magnetic fields (panel (b)) from a less-efficient turbulent dynamo (cf. Kim & Ostriker 2015b).

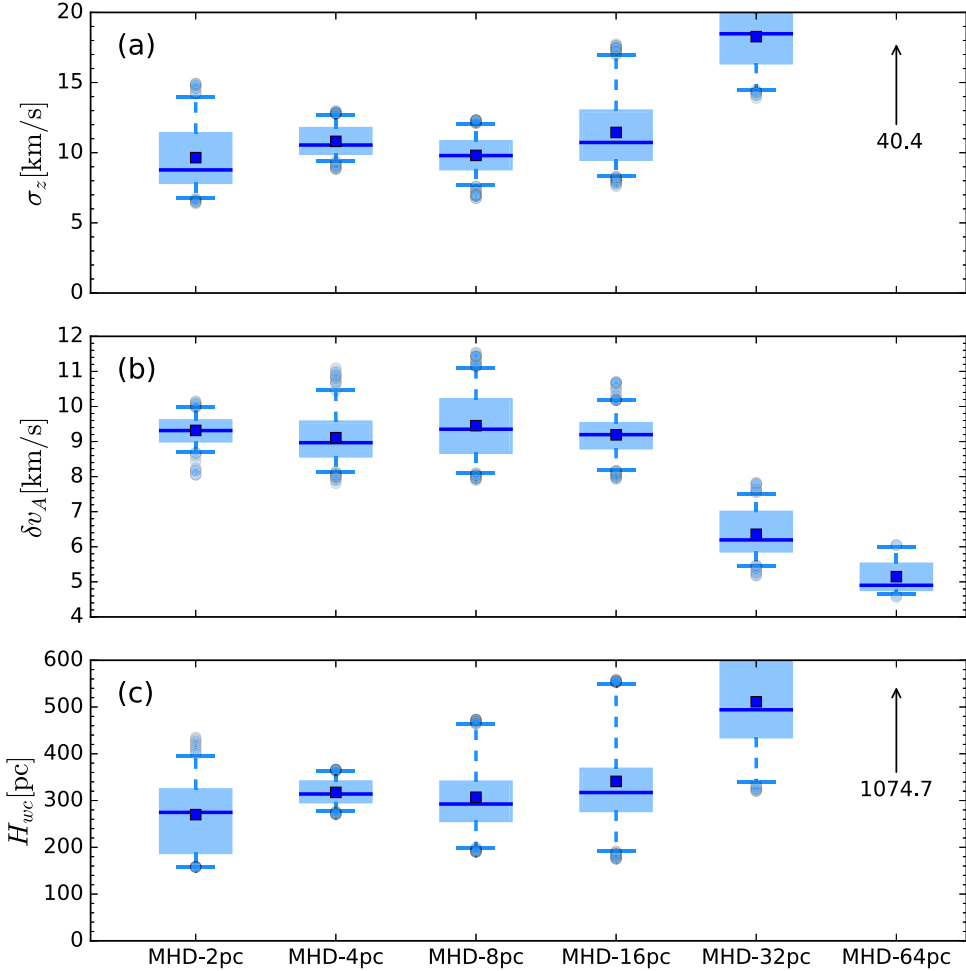


**Figure 16.** Dependence of ISM kinetic and magnetic properties on numerical resolution. Models with resolution  $\Delta x \leq 16$  pc are converged. Box-and-whisker plots of (a) vertical velocity dispersion, (b) turbulent Alfvén velocity, and (c) scale height of the warm–cold medium. Boxes enclose the 25th to 75th percentiles with medians and means shown as horizontal bars and squares, respectively. Whiskers extend to the 5th and 95th percentiles with outliers shown as circles. Note that in (a) and (c), Model MHD-64pc has extreme deviation from the converged results, so we simply indicate mean values with arrows.

To better understand resolution dependence of phase balance, we compare the box-and-whisker plot for statistics in the time range ( $t_{11}, t_9$ ). Figure 17 shows (a) the volume fraction of the hot gas within the scale height of the warm–cold medium, (b) the volume fraction of the WNM outside of  $|z| > 1.5$  kpc, and (c) the mass fraction of the CNM+UNM. These properties are essentially converged for Models MHD-8pc to MHD-2pc. However, as was previously evident from Figure 13, exaggeration of spatial and temporal correlations of SNe in Models MHD-32pc and MHD-64pc quickly blows everything away from the midplane. Model MHD-64pc effectively suffers “thermal runaway” (e.g., Li et al. 2015), so the hot gas occupies most of the volume (see Figure 13).

The total CNM+UNM mass fractions are more or less similar ( $f_{M,c+u} \sim 20\%-30\%$ ) up to Model MHD-16pc in terms of the mean and median, but we can see a decreasing median and increasing scatter as the resolution gets poorer. We note (not shown) that the mass fraction of the CNM alone keeps increasing at higher resolution, presumably due to a reduction in numerical diffusion that otherwise broadens the phase transition layer between the CNM and WNM (artificially turning CNM into UNM). We also note that, in low-resolution models, sink/star particles may form at a density that is insufficient to guarantee true collapse of the CNM (see Figure 3).

#### 4.4. Mass Loss Rates

We measure the areal mass-loss rates of each phase at different heights using outgoing fluxes

$$\dot{\Sigma}_{\text{wind},C}(|z|) \equiv \frac{\sum_c [(\rho v_{z,+})_{z+} - (\rho v_{z,-})_{z-}] \Delta V}{L_x L_y}, \quad (32)$$

where the outgoing velocity  $v_{z,\pm}$  denotes positive or negative velocity for positive or negative vertical coordinate  $z_\pm$ , respectively. Figure 18 plots the areal mass loss rates measured at  $|z| = 1$  kpc and 2 kpc in blue and green boxes and whiskers, respectively. Overall convergence is again seen for Models MHD-2pc to MHD-8pc. Models MHD-32pc and MHD-64pc are inconsistent with the mass fluxes in the resolved models.

As Martizzi et al. (2016) pointed out, the full evolution of galactic winds cannot be followed in local Cartesian box simulations. However, local simulations are very useful for investigating the launching condition of winds, especially because they afford very high resolution of multiphase gas and its heating and acceleration in SN remnants and superbubbles. By analyzing the outflowing gas properties for each phase, we are able to understand which material can escape and which cannot. In a companion paper, we shall conduct full analysis

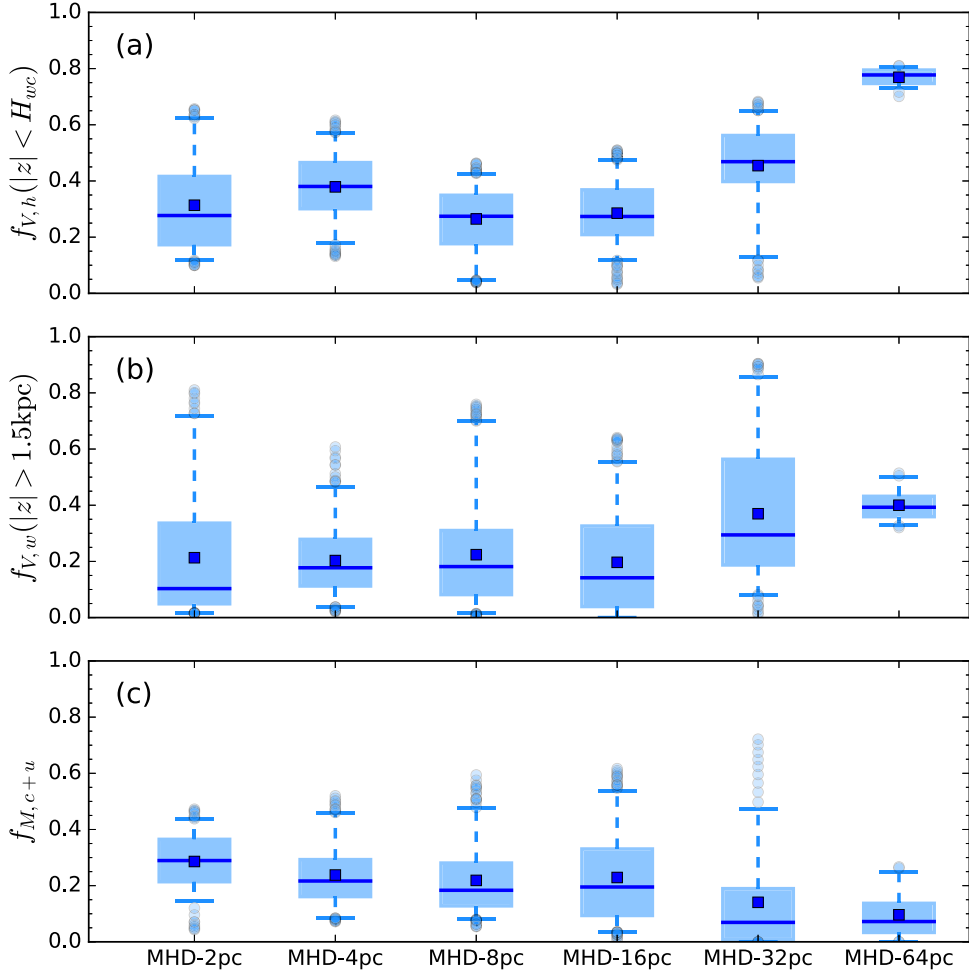


**Figure 17.** Dependence of ISM phase properties on numerical resolution. Models with resolution  $\Delta x \leq 16$  pc are converged. Box-and-whisker plots of (a) volume fraction of the hot gas within the scale height of the warm-cold medium, (b) volume fraction of the WNM outside of  $|z| > 1.5$  kpc, and (c) mass fraction of the CNM+UNM. Boxes enclose the 25th to 75th percentiles with medians and means shown as horizontal bars and squares, respectively. Whiskers extend to the 5th and 95th percentiles with outliers shown as circles.

using the Bernoulli parameter. Here, we simply consider convergence based on the mass loss rates measured at different  $|z|$ . If some of the material passing through  $|z| = 1$  kpc eventually falls back before it reaches the vertical boundaries at  $|z| = 2$  kpc, the mass loss rate is higher at lower  $|z|$ . This behavior is characteristic of a fountain flow, and is clearly evident for the WNM of the resolved models in Figure 18(c). However, the hot gas has high enough velocity to escape the galactic disk as a wind, and mass fluxes are nearly the same at  $|z| = 1$  kpc and  $|z| = 2$  kpc.

From Figure 14, the mean SFR surface density for the parameters of the present simulation is  $\Sigma_{\text{SFR}} \sim 5 \times 10^{-3} M_{\odot} \text{ kpc}^{-2} \text{ yr}^{-1}$ . In comparison, the mass loading factors ( $\beta_C \equiv \dot{\Sigma}_{\text{wind},C}/\Sigma_{\text{SFR}}$ ) of the hot and ionized gas are around  $\beta_h \sim \beta_i \sim 0.1$ . This is consistent with the expected range of hot gas mass loading factor for superbubbles that break out of the disk after shell formation, the typical situation (Kim et al. 2017). More heavily loaded winds are expected only if (1) the galactic gravitational potential well is shallow enough for the moderate-velocity WNM that is in cooled shells around superbubbles to escape, as may occur in dwarf galaxies, or (2) a very high local SN rate creates a superbubble that breaks

out of the ISM before cooling, as may occur in some nuclear starbursts (Kim et al. 2017).

## 5. Summary

In this paper, we have presented the TIGRESS algorithms that we have designed and implemented in the Athena MHD code, in order to conduct self-consistent simulations of the three-phase star-forming ISM in a wide range of galactic disk environments. We also demonstrate application of these algorithms to a fiducial model representing conditions in the solar neighborhood, and conduct a resolution study to assess requirements for convergence. In TIGRESS, the MHD equations are solved in a local frame that includes sheared galactic rotation, and augmented with optically thin cooling and heating, self- and external gravity, and modules to follow star formation and the feedback it engenders. The last two elements are implemented using sink/star particles to form star clusters within gravitationally collapsing gas, and to follow the FUV radiation and SN events that these clusters produce based on an adopted population synthesis model. Our implementation allows for runaway OB stars that may result from an SN in a massive binary system.

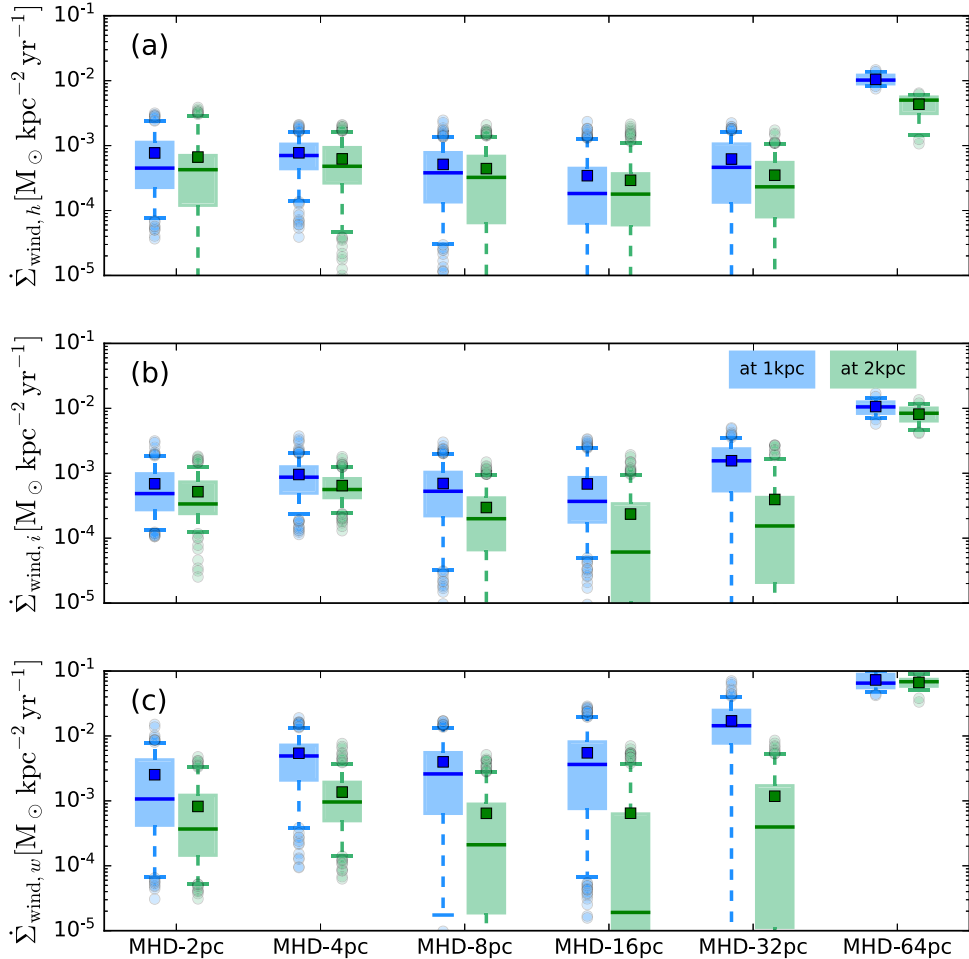


**Figure 18.** Dependence of wind mass-loss rates on numerical resolution. Models with resolution  $\Delta x \leq 8 \text{ pc}$  are converged. Box-and-whisker plots of areal mass loss rate statistics in units of  $M_{\odot} \text{kpc}^{-2} \text{yr}^{-1}$  for (a) hot gas  $\Sigma_{\text{wind},h}$ , (b) ionized gas  $\Sigma_{\text{wind},i}$ , and (c) warm gas  $\Sigma_{\text{wind},w}$ . Boxes enclose the 25th to 75th percentiles, with medians and means shown as horizontal bars and squares, respectively. Whiskers extend to the 5th and 95th percentiles, with outliers shown as circles. For each model, we plot two mass loss rates measured at  $|z| = 1 \text{ kpc}$  and  $|z| = 2 \text{ kpc}$ .

A key aspect of TIGRESS is the detailed treatment of sink/star particle formation and evolution. In Section 2.2, we delineate how we create, age, accrete onto, and move sink/star particles, and present tests for our implementation. Another key aspect is our approach to SN feedback. Our implementation treats SN explosions in three different ways (feedback types EJ, ST, and MC), depending on the mass of gas that is resolved in the immediate vicinity of the SN (see Section 2.3.3). This allows us to properly model creation of the hot ISM when the Sedov–Taylor stage of evolution can be resolved (which is usually possible, one of the main advantages of local simulations). If the Sedov–Taylor stage cannot be resolved, we inject momentum to the warm-cold ISM surrounding a SN based on the results of KO15a for the post-radiative stage. Our SN feedback prescription has proven to be quite robust, which has enabled us to run for extended evolution times (700 Myr, compared to only  $\sim 100$  Myr in some other recent simulations with self-gravity and SN feedback).

By carefully treating star formation and feedback, TIGRESS simulations yield realistic, fully self-consistent three-phase ISM models with self-regulated star formation and galactic winds. For the fiducial solar neighborhood model with gas surface density of  $\sim 10 M_{\odot} \text{pc}^{-2}$ , we show that a quasi-steady saturated state is reached in our higher resolution simulations. In

particular, we show that the SFR, wind mass-loss rate, disk scale height, turbulent and Alfvénic velocity dispersions, and volume fractions of warm and hot phases are converged provided that the numerical resolution is at least  $\Delta x = 8 \text{ pc}$ , such that the Sedov–Taylor stage is resolved for most SN events.

In numerically converged models, the SFR surface density is self-regulated to  $\Sigma_{\text{SFR}} \sim 5 \times 10^{-3} M_{\odot} \text{kpc}^{-2} \text{yr}^{-1}$  with large cyclic fluctuations. For gas at  $T < 2 \times 10^4 \text{ K}$ , the mass-weighted velocity dispersions and turbulent Alfvén velocity are each  $\sim 10 \text{ km s}^{-1}$ . The scale heights of the CNM+UNM and WNM are  $\sim 80 \text{ pc}$  and  $\sim 360 \text{ pc}$ , respectively. Hot gas fills  $\sim 30\text{--}40\%$  of the volume near the midplane, while warm gas is mixed within the mostly hot medium at  $|z| > 1 \text{ kpc}$ . High-velocity hot gas can escape with a ratio of hot gas outflow rate to SFR (the wind “mass loading factor”) of  $\sim 0.1$ . The WNM cannot achieve high enough velocity to escape the Milky Way’s gravitational potential, and instead creates a fountain flow reaching to a few kpc from the midplane.

At low resolution ( $\Delta x \geq 16 \text{ pc}$ ), the detailed ISM properties as well as mean SFR cannot be properly captured. Of course, the resolution requirements we report here are particular to the solar neighborhood model. One may expect more stringent

resolution requirements for galactic disk environments where the dynamical space and timescales are shorter (e.g., Jeans length varies inversely with the square root of density, and the SN shell formation radius has similar dependence). Also, different prescriptions from those we describe for feedback and star formation (as well as other physics) may give different convergence trends that are difficult to predict. The quantitative resolution requirements for convergence must be evaluated for any specific parameter set and adopted physics prescriptions.

The TIGRESS algorithms are currently being applied in a suite of numerical simulations systematically exploring SFRs, ISM properties, and galactic winds in diverse galactic environments. Results of these models and analyses will be presented in companion papers.

We are grateful to the referee for a detailed report, which helped us to improve the manuscript. This work was supported by grant AST-1312006 from the National Science Foundation and grant NNX14AB49G from NASA. Simulations were performed on the computational resources supported by the PICSciE TIGRESS High Performance Computing Center at Princeton University, and by the NASA High-End Computing (HEC) Program through the NASA Advanced Supercomputing (NAS) Division at Ames Research Center.

**Software:** Athena (Stone et al. 2008), STARBURST99 (Leitherer et al. 1999), yt (Turk et al. 2011), astropy (Astropy Collaboration et al. 2013), matplotlib (Hunter 2007), numpy (van der Walt et al. 2011), IPython (Perez & Granger 2007), pandas (McKinney 2010).

## ORCID iDs

Chang-Goo Kim <https://orcid.org/0000-0003-2896-3725>  
 Eve C. Ostriker <https://orcid.org/0000-0002-0509-9113>

## References

- Agertz, O., & Kravtsov, A. V. 2016, *ApJ*, **824**, 79  
 Agertz, O., Kravtsov, A. V., Leitner, S. N., & Gnedin, N. Y. 2013, *ApJ*, **770**, 25  
 Astropy Collaboration, Robitaille, T. P., Tollerud, E. J., et al. 2013, *A&A*, **558**, A33  
 Bai, X.-N., & Stone, J. M. 2010, *ApJS*, **190**, 297  
 Behroozi, P. S., Wechsler, R. H., & Conroy, C. 2013, *ApJ*, **770**, 57  
 Blaauw, A. 1961, *BAN*, **15**, 265  
 Cioffi, D. F., McKee, C. F., & Bertschinger, E. 1988, *ApJ*, **334**, 252  
 Cox, D. P., & Smith, B. W. 1974, *ApJL*, **189**, L105  
 Crain, R. A., Schaye, J., Bower, R. G., et al. 2015, *MNRAS*, **450**, 1937  
 Dale, J. E. 2015, *NewAR*, **68**, 1  
 Dalla Vecchia, C., & Schaye, J. 2012, *MNRAS*, **426**, 140  
 Davé, R., Thompson, R., & Hopkins, P. F. 2016, *MNRAS*, **462**, 3265  
 de Avillez, M. A. 2000, *MNRAS*, **315**, 479  
 de Avillez, M. A., & Breitschwerdt, D. 2004, *A&A*, **425**, 899  
 Draine, B. T. 1978, *ApJS*, **36**, 595  
 Eldridge, J. J., Langer, N., & Tout, C. A. 2011, *MNRAS*, **414**, 3501  
 Federrath, C., Chabrier, G., Schober, J., et al. 2011, *PhRvL*, **107**, 114504  
 Field, G. B. 1965, *ApJ*, **142**, 531  
 Field, G. B., Goldsmith, D. W., & Habing, H. J. 1969, *ApJL*, **155**, L149  
 Foster, P. N., & Chevalier, R. A. 1993, *ApJ*, **416**, 303  
 Frank, A., Ray, T. P., Cabrit, S., et al. 2014, in Protostars and Planets VI, ed. H. Beuther et al. (Tucson, AZ: Univ. Arizona Press), 451  
 Fujii, M. S., & Portegies Zwart, S. 2011, *Sci*, **334**, 1380  
 Gammie, C. F. 2001, *ApJ*, **553**, 174  
 Gatto, A., Walch, S., Low, M.-M. M., et al. 2015, *MNRAS*, **449**, 1057  
 Gatto, A., Walch, S., Naab, T., et al. 2017, *MNRAS*, **466**, 1903  
 Gent, F. A., Shukurov, A., Fletcher, A., Sarson, G. R., & Mantere, M. J. 2013, *MNRAS*, **432**, 1396  
 Girichidis, P., Walch, S., Naab, T., et al. 2016, *MNRAS*, **456**, 3432  
 Gong, H., & Ostriker, E. C. 2009, *ApJ*, **699**, 230  
 Gong, H., & Ostriker, E. C. 2011, *ApJ*, **729**, 120  
 Gong, H., & Ostriker, E. C. 2013, *ApJS*, **204**, 8  
 Gong, M., & Ostriker, E. C. 2015, *ApJ*, **806**, 31  
 Gong, M., Ostriker, E. C., & Wolfire, M. G. 2017, *ApJ*, **843**, 38  
 Heger, A., Fryer, C. L., Woosley, S. E., Langer, N., & Hartmann, D. H. 2003, *ApJ*, **591**, 288  
 Hennebelle, P., & Ifrig, O. 2014, *A&A*, **570**, A81  
 Hill, A. S., Joung, M. R., Mac Low, M.-M., et al. 2012, *ApJ*, **750**, 104  
 Hockney, R. W., & Eastwood, J. W. 1981, Computer Simulation Using Particles (New York: McGraw-Hill)  
 Hopkins, P. F., Kereš, D., Oñorbe, J., et al. 2014, *MNRAS*, **445**, 581  
 Hunter, J. D. 2007, *CSE*, **9**, 90  
 Ifrig, O., & Hennebelle, P. 2015, *A&A*, **576**, A95  
 Joung, M. K. R., & Mac Low, M.-M. 2006, *ApJ*, **653**, 1266  
 Katz, N. 1992, *ApJ*, **391**, 502  
 Keller, B. W., Wadsley, J., & Couchman, H. M. P. 2016, *MNRAS*, **463**, 1431  
 Kennicutt, R. C., Jr. 1998, *ApJ*, **498**, 541  
 Kim, C.-G., Kim, W.-T., & Ostriker, E. C. 2008, *ApJ*, **681**, 1148  
 Kim, C.-G., Kim, W.-T., & Ostriker, E. C. 2010, *ApJ*, **720**, 1454  
 Kim, C.-G., Kim, W.-T., & Ostriker, E. C. 2011, *ApJ*, **743**, 25  
 Kim, C.-G., & Ostriker, E. C. 2015a, *ApJ*, **802**, 99  
 Kim, C.-G., & Ostriker, E. C. 2015b, *ApJ*, **815**, 67  
 Kim, C.-G., Ostriker, E. C., & Kim, W.-T. 2013, *ApJ*, **776**, 1  
 Kim, C.-G., Ostriker, E. C., & Raileanu, R. 2017, *ApJ*, **834**, 25  
 Kim, W.-T., Ostriker, E. C., & Stone, J. M. 2002, *ApJ*, **581**, 1080  
 Kimm, T., & Cen, R. 2014, *ApJ*, **788**, 121  
 Korpi, M. J., Brandenburg, A., Shukurov, A., Tuominen, I., & Nordlund, Å. 1999, *ApJL*, **514**, L99  
 Koyama, H., & Inutsuka, S.-i. 2002, *ApJL*, **564**, L97  
 Koyama, H., & Ostriker, E. C. 2009, *ApJ*, **693**, 1316  
 Kroupa, P. 2001, *MNRAS*, **322**, 231  
 Krumholz, M. R., Bate, M. R., Arce, H. G., et al. 2014, in Protostars and Planets VI, ed. H. Beuther et al. (Tucson, AZ: Univ. Arizona Press), 243  
 Kuijken, K., & Gilmore, G. 1989, *MNRAS*, **239**, 571  
 Larson, R. B. 1969, *MNRAS*, **145**, 271  
 Leitherer, C., Schaerer, D., Goldader, J. D., et al. 1999, *ApJS*, **123**, 3  
 Lemaster, M. N., & Stone, J. M. 2009, *ApJ*, **691**, 1092  
 Leroy, A. K., Bigiel, F., de Blok, W. J. G., et al. 2012, *AJ*, **144**, 3  
 Li, M., Bryan, G. L., & Ostriker, J. P. 2017, *ApJ*, **841**, 101  
 Li, M., Ostriker, J. P., Cen, R., Bryan, G. L., & Naab, T. 2015, *ApJ*, **814**, 4  
 Lopez, L. A., Krumholz, M. R., Bolatto, A. D., et al. 2014, *ApJ*, **795**, 121  
 Mac Low, M.-M., & Klessen, R. S. 2004, *RvMP*, **76**, 125  
 Martizzi, D., Faucher-Giguère, C.-A., & Quataert, E. 2015, *MNRAS*, **450**, 504  
 Martizzi, D., Fielding, D., Faucher-Giguère, C.-A., & Quataert, E. 2016, *MNRAS*, **459**, 2311  
 McKee, C. F., & Ostriker, E. C. 2007, *ARA&A*, **45**, 565  
 McKee, C. F., & Ostriker, J. P. 1977, *ApJ*, **218**, 148  
 McKinney, W. 2010, in Proc. 9th Python in Science Conf., Data Structures for Statistical Computing in Python, ed. S. van der Walt & J. Millman (Austin, TX: SciPy), 51  
 Moster, B. P., Naab, T., & White, S. D. M. 2013, *MNRAS*, **428**, 3121  
 Oh, S., Kroupa, P., & Pfleiderer-Altenburg, J. 2015, *ApJ*, **805**, 92  
 Ostriker, E. C., McKee, C. F., & Leroy, A. K. 2010, *ApJ*, **721**, 975  
 Ostriker, E. C., & Shetty, R. 2011, *ApJ*, **731**, 41  
 Penston, M. V. 1969, *MNRAS*, **144**, 425  
 Perez, F., & Granger, B. E. 2007, *CSE*, **9**, 21  
 Peters, T., Naab, T., Walch, S., et al. 2017, *MNRAS*, **466**, 3293  
 Portegies Zwart, S. F. 2000, *ApJ*, **544**, 437  
 Poveda, A., Ruiz, J., & Allen, C. 1967, *BOTT*, **4**, 86  
 Quinn, T., Perrine, R. P., Richardson, D. C., & Barnes, R. 2010, *AJ*, **139**, 803  
 Raskutti, S., Ostriker, E. C., & Skinner, M. A. 2016, *ApJ*, **829**, 130  
 Rosdahl, J., Schaye, J., Dubois, Y., Kimm, T., & Teyssier, R. 2017, *MNRAS*, **466**, 11  
 Sanders, R., Morano, E., & Druguet, M.-C. 1998, *JCoPh*, **145**, 511  
 Schaye, J., Crain, R. A., Bower, R. G., et al. 2015, *MNRAS*, **446**, 521  
 Schober, J., Schleicher, D., Federrath, C., et al. 2012, *ApJ*, **754**, 99  
 Somerville, R. S., & Davé, R. 2015, *ARA&A*, **53**, 51  
 Sternberg, A., McKee, C. F., & Wolfire, M. G. 2002, *ApJS*, **143**, 419  
 Stone, J. M., & Gardiner, T. 2009, *NewA*, **14**, 139  
 Stone, J. M., & Gardiner, T. A. 2010, *ApJS*, **189**, 142  
 Stone, J. M., Gardiner, T. A., Teuben, P., Hawley, J. F., & Simon, J. B. 2008, *ApJS*, **178**, 137  
 Sutherland, R. S., & Dopita, M. A. 1993, *ApJS*, **88**, 253

- Tammann, G. A., Loeffler, W., & Schroeder, A. 1994, *ApJS*, **92**, 487  
Teyssier, R., Pontzen, A., Dubois, Y., & Read, J. I. 2013, *MNRAS*, **429**, 3068  
Thornton, K., Gaudlitz, M., Janka, H.-T., & Steinmetz, M. 1998, *ApJ*, **500**, 95  
Truelove, J. K., Klein, R. I., McKee, C. F., et al. 1997, *ApJL*, **489**, L179  
Turk, M. J., Smith, B. D., Oishi, J. S., et al. 2011, *ApJS*, **192**, 9  
van der Walt, S., Colbert, S. C., & Varoquaux, G. 2011, *CSE*, **13**, 22  
Vogelsberger, M., Genel, S., Springel, V., et al. 2014, *Natur*, **509**, 177  
Vorobyov, E. I., & Basu, S. 2005, *MNRAS*, **360**, 675  
Walch, S., Girichidis, P., Naab, T., et al. 2015, *MNRAS*, **454**, 238  
Walch, S., & Naab, T. 2015, *MNRAS*, **451**, 2757  
Wang, P., Li, Z.-Y., Abel, T., & Nakamura, F. 2010, *ApJ*, **709**, 27  
Zhang, L., Rix, H.-W., van de Ven, G., et al. 2013, *ApJ*, **772**, 108